Spectroscopy of the highly neutron-deficient N=84 isotones ^{160}Os and ^{159}Re

Thesis submitted in accordance with the requirements of the University of Liverpool for the degree of Doctor in Philosophy

by

Alexander Gredley

Oliver Lodge Laboratory

September 2017

Acknowledgements

Firstly, I would like to thank Prof. Robert Page for giving me the opportunity to undertake this research. Robert always found the time to help and his guidance was invaluable. His expertise is second to none and I could not have asked for a better supervisor.

Sincere thanks also go to Prof. David Joss for being instrumental in convincing me to do a PhD and for all his support, including many informative chats.

Thank you to the STFC for providing funding, to everyone at the University of Jyväskylä accelerator lab, and all the staff at Liverpool who made this work possible. Thanks also to Drs. Eddie Parr and John Revill for getting me started and for their help in troubleshooting when things weren't going smoothly.

I have thoroughly enjoyed my time as a PhD student and that is due in no small part to the other students in the Nuclear Physics group, both past and present. Thank you for the coffee breaks, the Friday nights, and all the support when things went wrong. Special thanks go to Dr. Faye Wearing: it's been a long journey, but it wouldn't have been the same without you.

Thank you also to James Hunt, whose friendship over the years has meant more than he knows; to Polett Bali for her love and support in the final months of my PhD; and to my parents, for everything.

Abstract

Neutron deficient N=84 isotones have been synthesised in ^{106}Cd (^{58}Ni) fusion evaporation reactions in an experiment performed at the University of Jyväskylä accelerator laboratory. Reaction products were identified and their properties measured using the GREAT spectrometer in conjunction with the RITU gas-filled separator and the LISA spectrometer, while the Jurogam II spectrometer was used to measure γ rays emitted at the target position.

Mother-daughter correlations have been used to produce evidence for the first observation of α decay from the ground state of ^{160}Os. The Q-value and half-life of the signal were measured to be 7415 (50) keV and 35^{+19}_{-15} μs, respectively. No evidence of the expected 8^+ isomer was found. Further experimental work at the University of Jyväskylä has been approved on the strength of this work.

Improved measurements of the decay properties of $h_{11/2}$ state in ^{159}Re and ^{155}Ta have been performed. The half-life of this state in ^{159}Re was measured to be 21(1) μs. The decay energy and branching ratios were 6818(6) keV and 5.0(8)% for the α decay branch and 1802(5) keV and 95(4) % for the proton decay branch. The proton decay of ^{155}Ta was measured to have an energy of 1429(5) keV and a half-life of 3.3(6) ms. All values are consistent with previous works.

γ rays above the $h_{11/2}$ state in ^{159}Re were identified for the first time and

comparisons to the odd-Z isotone ^{157}Ta were used to deduce the order of the lowest lying of these γ rays. Evidence for the expected α-decaying $25/2^-$ isomer was found.

Contents

1 Introduction **7**

1.1 Background and Motivation 8

1.2 Spectroscopy of ^{160}Os and ^{159}Re 13

2 Physics Background **15**

2.1 Nuclear Models 15

2.1.1 The Liquid Drop Model 15

2.1.2 The Shell model 17

2.2 The Drip Lines 21

2.3 Alpha Decay 22

2.4 Proton Emission 27

2.5 Beta Decay and Electron Capture 28

2.6 Gamma Decay 31

3 Experimental Apparatus **33**

3.1 Apparatus 33

3.1.1 JUROGAM II germanium array 34

3.1.2 LISA 35

3.1.3 RITU 36

3.1.4 The GREAT spectrometer 38

3.2 Total Data Readout (TDR) 40

4 Experimental Methods **42**

4.1 Fusion-evaporation reactions 42

4.2 Particle discrimination 44

4.3 Calibrations 45

4.4 Doppler-Shift correction 48

4.5 Background Suppression with the PIN Diodes 49

4.6 LISA as a channel selector 53

5 Evidence for the alpha decay of ^{160}Os **57**

5.1 Results 57

5.1.1 LISA veto 63

5.1.2 Q-value 65

5.1.3 Background analysis 66

5.1.4 Half-Life 69

5.1.5 Production cross Section 72

5.1.6 Contribution from ^{156}Ta proton correlation 72

5.1.7 Search for the Expected 8^+ Isomer 75

6 Spectroscopy of ^{159}Re and ^{155}Ta **77**

6.1 Results 79

6.1.1 Improved spectroscopic measurements of known α and proton decays 79

6.1.2 γ rays above the $h_{11/2}$ state 82

6.1.3 Search for the Expected $25/2^-$ Isomer 82

7 Discussion **86**

7.1 ^{160}Os Assignment 86

7.1.1 High spin isomer in the N=84 isotones 88

7.1.2 Decays emanating from a ^{159}Re $h_{11/2}$ orbital 89

8 Summary **93**

Chapter 1

Introduction

Our understanding of the nuclear system is still far from complete and the ongoing effort to identify and measure the properties of nuclides is done with the goal of refining the models with which we attempt to describe the nucleus. One approach involves the characterisation of nuclei far from stability, since these provide a stringent test for models that were developed using knowledge of nuclei close to β stability. Figure 1.1 shows a small section of the chart of nuclei including the nuclei relevant to this work.

The nuclides on which this work focuses are highly neutron-deficient N=84 isotones which lie two neutrons above the N=82 shell closure close to the proton drip line. To date, the heaviest known N=84 isotone is ^{159}Re. In order of decreasing mass the next four isotones are ^{158}W, ^{157}Ta, ^{156}Hf and ^{155}Lu. This thesis presents the search for ^{160}Os which would represent the next isotone above ^{159}Re, as well as spectroscopic measurements of ^{159}Re and improved measurements for the proton emission of the closed neutron shell nucleus ^{155}Ta, which is the α decay daughter of ^{159}Re.

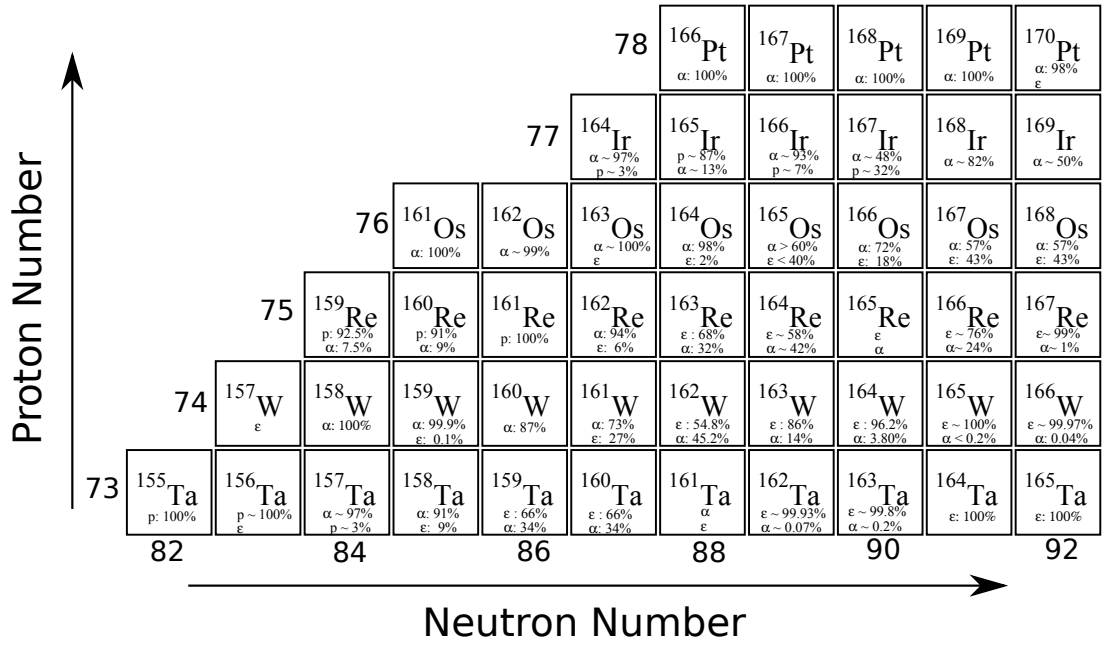

Figure 1.1: *A small section of the chart of nulcides, showing the nuclei relevent to this work. Decay data is for the lowest lying known charged particle emitting states. Modified from reference [1].*

1.1 Background and Motivation

Of the 39 known isotopes of osmium, seven are stable. The discovery of ^{161}Os by Bianco et al. [2] represents the lightest previously discovered isotope of osmium, having 23 fewer neutrons than the nearest stable isotope. This work presents evidence of ^{160}Os. There are predicted to be two further isotopes (^{158,159}Os) that are bound against single particle emission [3].

Figure 1.2 shows the strong dependence of half-life on neutron number for even-Z neutron-deficient nuclei, as well as the abrupt change from β decay to α decay as the N=82 shell closure is approached. In the case of the osmium isotopes ^{160}Os (N=84) is expected to be the lightest α-decaying isotope [5] because beyond this α decay must remove neutrons from the N=82 closed

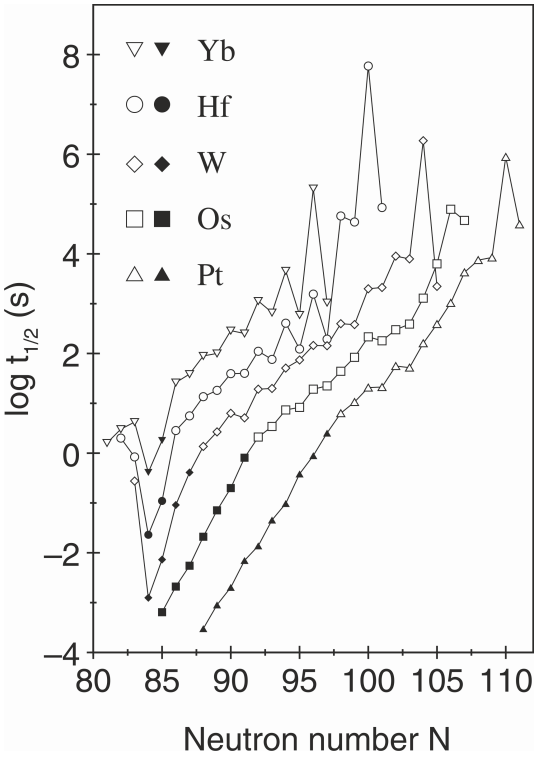

Figure 1.2: *The ground-state half-lives of Yb, Hf, W, Os and Pt isotopes as a function of neutron number. Nuclides in which α decay dominates are shown with filled symbols while nuclides in which β decay dominates are shown with hollow symbols. Data are taken from [4].*

shell resulting in a significant reduction in Q-value.

The neighbouring isotone of ^{160}Os with Z=75, N=84 is ^{159}Re. There are 38 known isotopes of rhenium, of which two are stable. The discovery of ^{159}Re was reported in reference [6] by Joss et al., and represents the lightest known isotope of rhenium. The proton emission of ^{155}Ta, the α decay daughter of ^{159}Re, was reported in reference [7] by Page et al. However, this work found only five counts and was in contradiction with a previous claim that reported a much higher energy proton emission from ^{155}Ta [8].

One of the factors that drives the motivation to study these nuclei is their proximity to the proton drip line. Proton radioactivity is an excellent probe of nuclear structure due to the strong dependence of the lifetime of proton

emitting states on the energy and angular momentum of the emitted proton. The predicted half-lives are also very sensitive to the nuclear deformation and residual interactions [9], and investigating nuclei where these factors are at a minimum provides useful information to study these phenomona. Figure 1.3 shows the calculated quadropole deformation parameters, β_2 of known proton emitters against neutron number. It shows data from two different theoretical models, the finite-range droplet model (FRDM) [10] and the Hartree-Fock-Boguliubov (HFB) method with a Skyrme interaction [11]. Both models predict ^{155}Ta to be the most spherical proton-emitting nucleus making it an ideal case to test theories of proton emission in spherical nuclei, and ^{159}Re is of similar interest with one of the lowest predicted deformations.

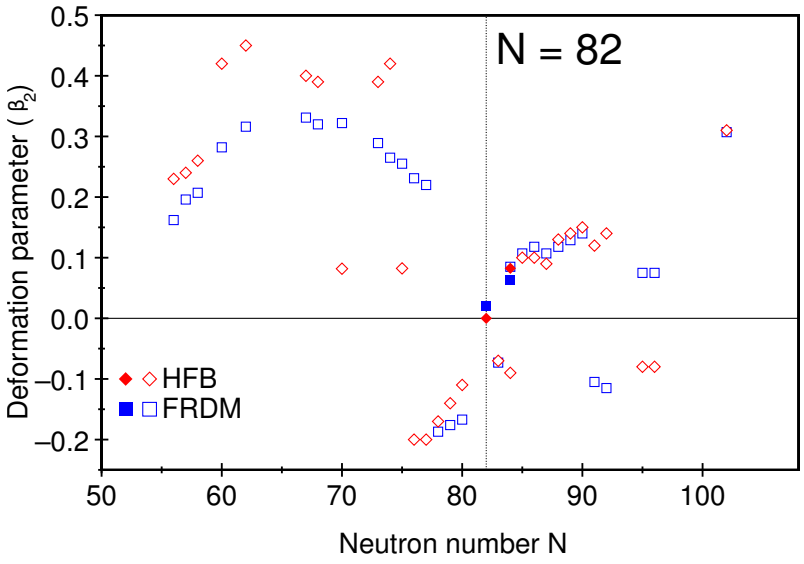

Figure 1.3: *Calculated deformation parameters of proton emitters as a function of their neutron number according to the finite-range droplet model [10] (blue) and the Hartree-Fock-Boguliubov method with a Skyrme interaction [11] (red). The proton emitters that are relevant to this work,* ^{155}*Ta and* ^{159}*Re, are indicated with filled squares.*

In addition to their proximity to the proton drip line nuclei in this region are

of interest as a probe for measuring the interactions between nuclear orbitals below the Z=82 and above the N=82 shell closures. It was reported in reference [12] that ^{146}Gd (N=82, Z=64) behaves like a doubly magic nucleus. The neutrons fill the N=82 shell closure while the stability of the proton shell is attributed to a large energy gap between the $g_{7/2}$, $d_{5/2}$ proton orbitals (filled in ^{146}Gd) and the remaining proton orbitals below the Z=82 major shell closure (i.e. $h_{11/2}$, $s_{1/2}$ and $d_{3/2}$). Nuclei with Z>64 and N=84 are therefore suitable for measurements of the interactions between the $\nu f_{7/2}$ and $\nu h_{9/2}$ orbitals, as well as the interaction between these neutron orbitals and the proton orbitals above $g_{7/2}$, $d_{5/2}$.

One result of previous measurements is the observation of spin-trap isomers observed in ^{158}W [13], ^{157}Ta [14], ^{156}Hf and ^{155}Lu [15]. In the even-even isotones the 8^+ state is a result of the broken neutron pair in the configuration $[\nu f_{7/2}h_{9/2}]$. The systematics of the heavier N=84 isotones, shown for the even-even isotones in figure 1.4, show a lowering of the excitation energy of the 8^+ state with respect to the 6^+ state, resulting in a higher excitation energy for the 6^+ state in ^{156}Hf and ^{158}W. This trend is attributed to the interaction between the $h_{9/2}$ neutron and the increasingly populated $\pi h_{11/2}$ orbital which causes a lowering of the energy gap between the $f_{7/2}$ and $h_{9/2}$ neutrons and a decrease in the excitation energy of the 8^+ state [16]. Meanwhile, the 6^+ state, in the configuration $\nu {f_{7/2}}^2$, increases steadily in excitation energy as proton pairs are added. When the 8^+ state falls below the 6^+ state a hindered E4 transition would be required for γ decay, and α decay becomes the dominant decay mode.

In the odd-Z isotones the isomer appears due to a similar mechanism as a $25/2^-$ state in a $[\pi h_{11/2}\nu f_{7/2}h_{9/2}]$ configuration. It should be noted that the assignment of the isomer to ^{157}Ta is tentative. It was reported in reference [14]

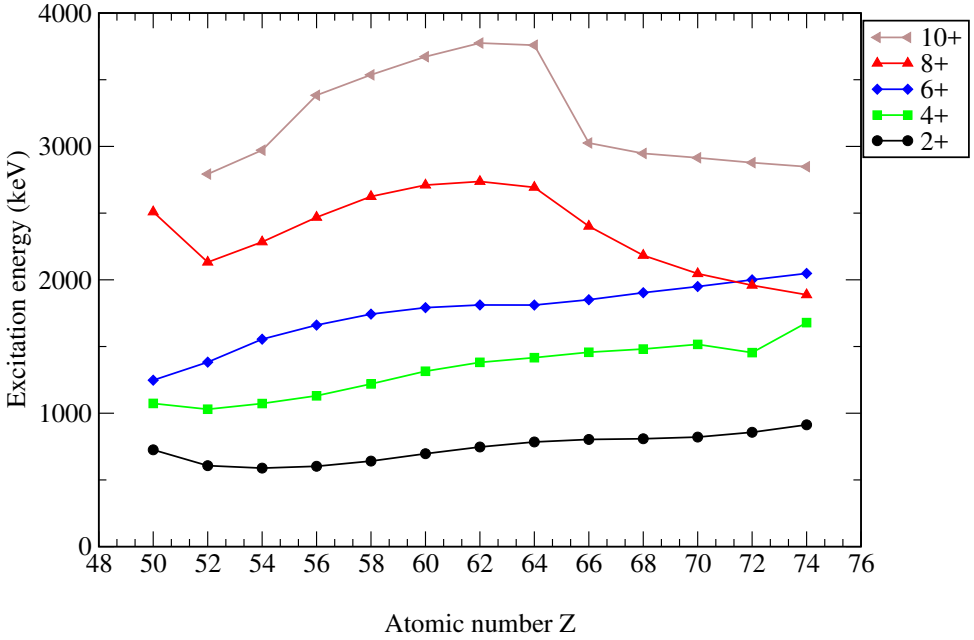

Figure 1.4: *Level systematics of the heavy even-even N=84 isotones. The crossing of the 8+ and 6+ states at Z=72 results in the 8+ isomer observed in* ^{156}*Hf and* ^{158}*W.*

that the decay curve of ^{156m}Hf has two distinct time components of 520(10) μs and 1.7(1) ms, the longer-lived of which is believed to correspond to an unresolved low-energy decay, and this decay was tentatively assigned to an ^{157m}Ta α decay. However, subsequent experiments have not confirmed this [16].

^{159}Re and ^{160}Os are both expected exhibit this same α-decaying isomer and the measurement or non-measurement is an important motivation for studying these nuclides. In the case of ^{160}Os it is also possible the the isomer will decay by two-proton emission. The ground state is predicted to be 2p unbound by 640 keV [5] and while the predicted Q-value is probably too low for 2p emission to be observed from the ground state there is a possibility that the excitation energy of the 8^+ state (potentially an additional 2 MeV) may be sufficient to allow it to undergo this rare decay mode. A similar case exists in the 8^+ isomer

of the N=84 isotone ^{158}W which suggests that other decay modes will dominate even given a negative 2p separation energy. From reference [17] and references therein the isomer in ^{158}W is predicted to be 2p unbound by 1478(530) keV, but no evidence of this decay mode was found with an upper limit on the branching ratio of 0.17% at the 90% confidence level.

1.2 Spectroscopy of ^{160}Os and ^{159}Re

Progress in studying these highly neutron-deficient nuclei is limited by the difficulties of synthesising them in a laboratory. The reaction used in this work was ^{58}Ni + ^{106}Cd to produce the compound nucleus ^{164}Os. ^{160}Os may then be produced in a 4-neutron evaporation channel while ^{159}Re is produced in a p4n channel and ^{155}Ta is produced as the α-decay daughter of ^{159}Re. Neutrons have a significantly higher binding energy than protons in this very proton rich region, leading to the favoured emission of protons and α particles over neutrons, in spite of the coulomb barrier which would usually hinder these emissions. Neutron-only evaporation channels therefore have very low cross sections in this region. A guide for the expected cross section of ^{160}Os can be found from ^{166}Pt, the lightest known Pt isotope, which was produced in reference [18] using the same 4-neutron evaporation channel with a cross section of 4 nb. Furthermore, in references [2] and [13] ^{161}Os and ^{162}Os were produced from the same compound nucleus with cross sections of 10 nb and 280 nb, respectively, and a similar reduction in cross section may be expected with each decrease in neutron number.

Chapter 2 describes the background physics theory that informs the work of this thesis. Chapters 3 and 4 describe the experimental apparatus and techniques used, including the recently commissioned LISA spectrometer and its

use in this work as a charged particle veto detector. Chapters 5 and 6 present the results of this work. A major challenge for identifying the α decay of ^{160}Os is the fragmented nature of daughter decays which results in several possible decay paths with varying half-lives and correlations. The methods used to contend with these challenges and the evidence accumulated are presented in chapter 5. The study of ^{159}Re is also hindered by a low production cross section and high background contamination. Chapter 6 presents spectroscopic measurements of the $h_{11/2}$ state in ^{159}Re and its α decay daughter, ^{155}Ta, as well as evidence for the expected ^{159}Re $25/2^-$ isomer and γ rays above the $h_{11/2}$ state. Some of the results presented in chapter 6 were produced in collaboration with Dr. Edward Parr, an account of the specific contributions from the collaborator is given in the chapter. The implications and significance of all these results are discussed in chapter 7. A summary of this work and a discussion of future work on this subject can be found in chapter 8.

Chapter 2

Physics Background

The atomic nucleus is system of protons and neutrons that interact through the strong, weak and electromagnetic forces, The result is a startlingly complex system, our understanding of which has been evolving for the last century.

2.1 Nuclear Models

2.1.1 The Liquid Drop Model

A relatively simple approach to describing the nucleus is motivated by the observation of the saturation of the nuclear force, in which the total binding energy of a nucleus is roughly proportional to the number of nucleons, A, rather than the total number of pairs of nuclei, A(A-1). This observation suggests that the nuclear interaction occurs only between neighbouring nucleons and leads to the liquid drop approach to modelling the nucleus, in which nuclei are treated as a spherical and incompressible fluid.

The mass of a nucleus containing Z protons and N neutrons is given by the equation

$$m = Zm_p + Nm_n - \frac{E_B}{c^2}, \tag{2.1}$$

where m_p, m_n, E_B and c are the proton mass, neutron mass, binding energy and speed of light respectively. The 'semi-empirical mass formula' describes the binding energy using five terms given by

$$E_B = a_V A - a_S A^{2/3} - a_C \frac{Z(Z-1)}{A^{1/3}} - a_A \frac{(A-2Z)^2}{A} - \delta(A,Z), \qquad (2.2)$$

where A=Z+N. The volume term arises because the Pauli Exclusion Principle prevents nucleons from occupying the same quantum state while the short range of the nuclear force means nucleons interact only with their nearest neighbours. There is consequently a positive contribution to the binding energy proportional to the number of nucleons. Nucleons at the surface, however, have fewer neighbours and contribute less to the total binding energy than nucleons in the centre. The surface term, proportional to the surface area, corrects for this effect.

The Coulomb term accounts for the electrostatic repulsion between the protons. It is proportional to the number of proton pairs (equal to Z(Z-1)) and inversely proportional to the radius of the nucleus.

The last two terms are quantum mechanical in nature and are a result of the Pauli Exclusion Principle. Nucleons are spin 1/2 fermions. Protons and neutrons are treated as having different isospin projections and are free to occupy the same energy state without violating the Pauli Exclusion Principle. Two nucleons with the same isospin projection number (i.e. two protons or two neutrons) may occupy the same state if their spins are aligned in anti-parallel, but additional nucleons of the same type are forced to occupy higher energy states. The asymmetry term accounts for the fact that a difference between a nucleus' N and Z numbers leads to decreased binding energy because the

excess protons or neutrons must occupy higher energy states compared to the nucleons in their symmetric isobars. The pairing term accounts for the fact that in a nucleus with an odd N and/or Z number there must be an unpaired neutron and/or proton, decreasing the overall binding energy. The pairing term is a positive contribution to the binding energy when Z and N are both even, no contribution for odd-A and a negative contribution when Z and N are both odd.

The liquid drop model does a good job of predicting the overall trend of binding energy per nucleon as a function of mass number. However, it fails to accurately reproduce the binding energy of light nuclei or deformed nuclei, and it cannot reproduce the shell effects observed for certain values of Z and N.

2.1.2 The Shell model

The shell structure of atomic electrons is the basis of modern chemistry and it is a natural step to search for similar structure in nuclei. The theoretical formulation must be different between the two situations since in electronic shell structure electrons move in an externally generated field (the Coulomb field of the nucleus) while the potential in which nucleons move is generated by their interactions with each other. Furthermore, electronic shell structure has well defined spatial characteristics in which the size of the electron is far smaller than the orbit it occupies. The size of the nucleon compared to the nucleus is much larger than that of the electron to the atom and the probability of nucleon-nucleon interactions would appear very high given the large spatial overlap. Nonetheless, experimental evidence for shell structure is abundant and a theoretical framework has been developed around these observations.

The fundamental assumption of the nuclear shell model is that nucleons

move in a mean potential generated by all other nucleons. Shell structure is characterised by the irregular distribution of level density with energy, leading to certain numbers of protons or neutrons which may be described as forming a 'closed shell', meaning that there is a large gap before the next available energy level. These numbers are described as magic numbers. From experiment, the magic numbers are 2, 8, 20, 28, 50 and 82 for both protons and neutrons. For neutrons 126 is magic, but this has not been verified for protons since we have not synthesised nuclei with such a high Z number.

The Pauli Principle allows nucleons within closed shells to be treated as independent particles with no nucleon-nucleon interactions because when an orbital is filled (i.e. the Pauli Exclusion Principle will allow no more nucleons to occupy that state) then any scattering process must excite a nucleon to a higher orbital. The energy required to excite the nucleons out of the shell is out of range of ordinary scattering ranges. This explains how multiple nucleons can occupy the same orbital without constant collision despite the relatively large size of the nucleon compared to the nucleus.

Solving the Shrödinger equation for a particle confined to the mean field potential gives the relative energy of the states available. When a spin-orbit interaction term is added to a potential that accurately represents the conditions inside the nucleus then the mag numbers are reproduced reproduces the magic numbers.

A simple choice is a harmonic oscillator of the form

$$V(r) = \frac{1}{2} m\omega^2 r^2, \tag{2.3}$$

where r is the three-dimensional position coordinate, m is the mass and ω is the harmonic oscillator frequency. The shape of this potential is shown

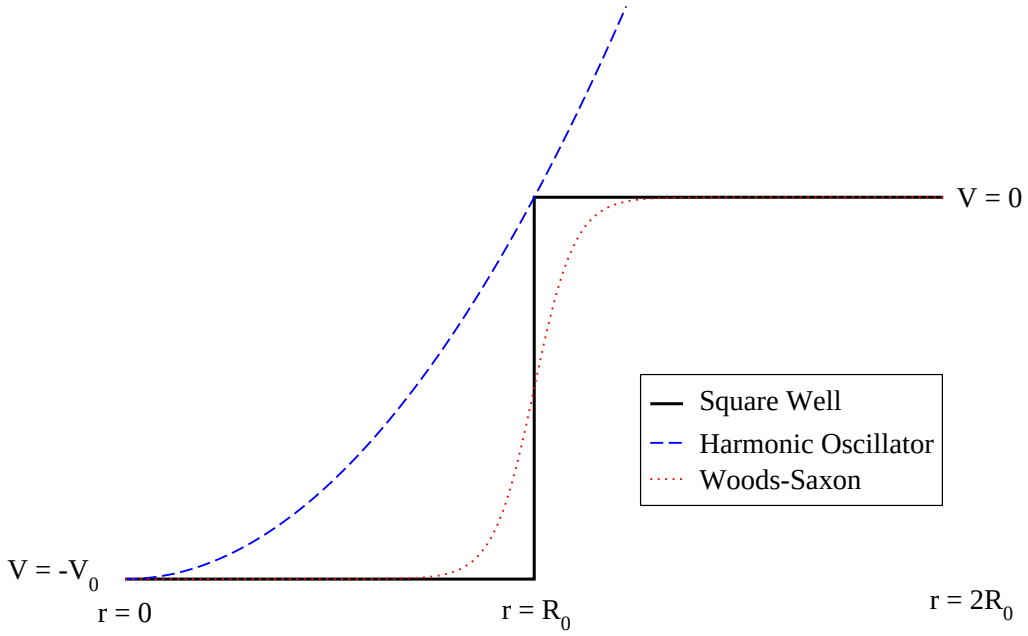

Figure 2.1: *Three possible nuclear mean field potentials.*

in figure 2.1, where it is compared with a square well potential and a Woods-Saxon potential. A state with angular momentum l in a simple harmonic oscillator potential has degeneracy arising from

$$m_l = -l, -l+1, ..., l-1, l, \tag{2.4}$$

and

$$m_s = \pm\frac{1}{2}, \tag{2.5}$$

giving a degeneracy of $2(2l+1)$. The energy levels obtained from this potential are shown on the left part of figure 2.2. The first three magic numbers (2,8,20) are correctly predicted using a harmonic oscillator potential [19].

High l orbits are more likely to be found at large values of r, therefore

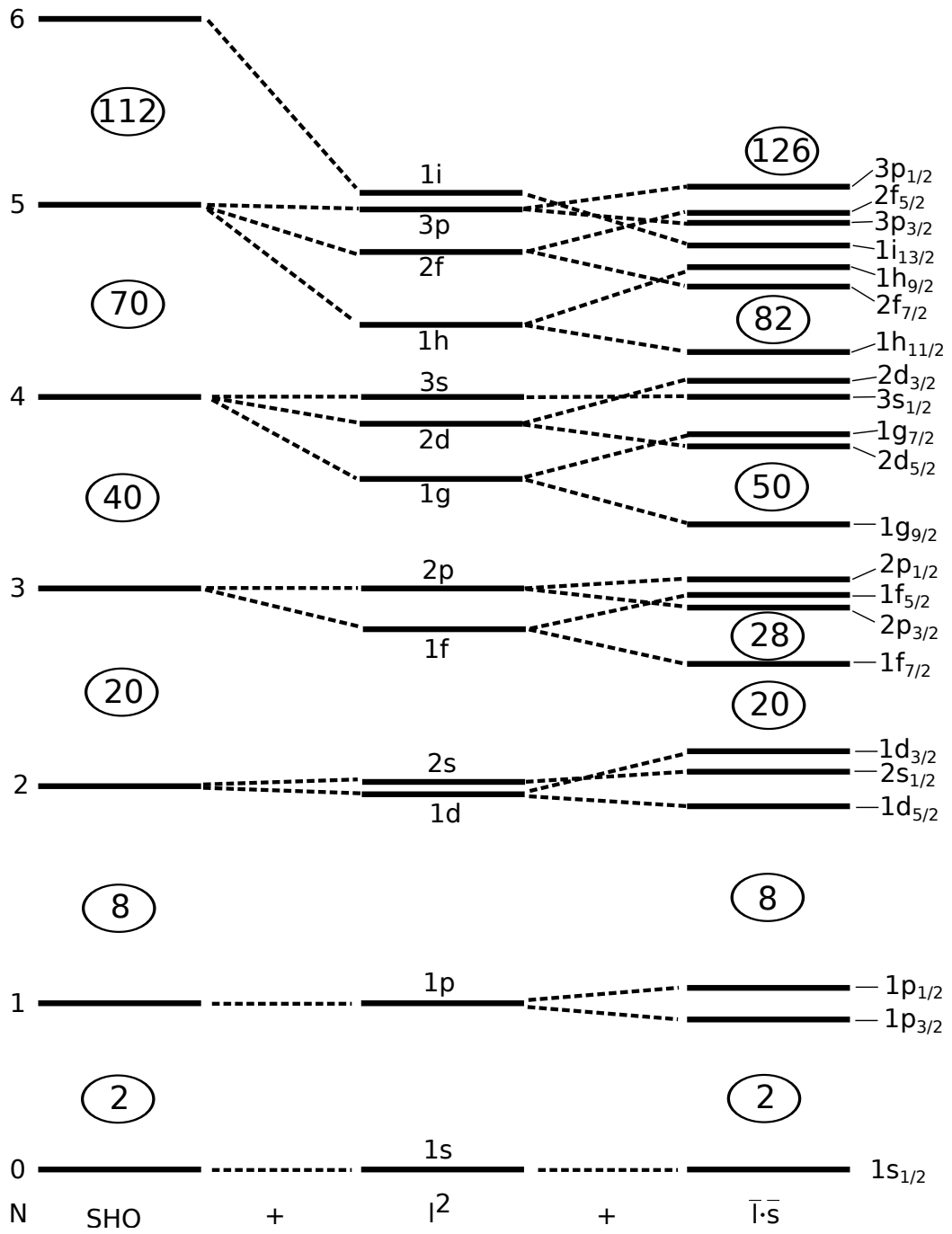

Figure 2.2: *Energy levels for a simple harmonic oscillator potential (left), a modified SHO potential with an l^2 term (middle) and a realistic potential with an l^2 term and a spin orbit term (right).*

adding an l^2 term results in a more attractive potential at large r and a flatter potential at small r. This better describes the nuclear potential in which nucleons well within the nuclear radius are surrounded isotropically by other nucleons and feels no net force. The l^2 term breaks the l degeneracy of the major shells for $l > 1$, as shown in the middle part of figure 2.2.

The addition of a spin-orbit term has the effect of splitting each nl level into two, depending on whether the intrinsic spin is aligned parallel or anti-parallel to the orbital angular momentum. The result is shown in the right hand part of figure 2.2 in which all the magic numbers are correctly reproduced. However, the shape of a harmonic oscillator potential does not accurately reflect the short range nature of the nuclear force.

A Woods-Saxon potential has the form

$$V(r) = \frac{-V_0}{1 + exp[(r - R)/a]}, \tag{2.6}$$

where R is the mean radius and a is a diffuseness parameter and varies the distance over which the transition from V_0 and 0 occurs. The Woods-Saxon potential resembles a combination of a square well and harmonic oscillator potentials (see figure 2.1). If the l^2 and spin-orbit corrections are applied to a Woods-Saxon potential it correctly reproduces the magic numbers [20] and is a more realistic description of the potential inside the nucleus, i.e. constant potential for nucleons well below the nuclear surface and then a smooth transition to zero outside at the surface.

2.2 The Drip Lines

A general principle of experimental physics is that extreme values of a given variable provide the most stringent tests of physical models relating to that

variable. One such case in nuclear physics is the limit of nuclear binding at extremes of isospin, known as the nuclear drip line.

The proton and neutron single particle separation energies are given by:

$$S_p(A,Z) = B(A,Z) - B(A-1,Z-1) \tag{2.7}$$

$$S_n(A,Z) = B(A,Z) - B(A-1,Z) \tag{2.8}$$

where B is the binding energy of a nucleus with given A and Z numbers. The lines along the nuclear chart where these values go to zero are the proton and neutron drip lines, respectively, and nuclides beyond the drip line are unbound to proton or neutron emission.

It is possible to perform spectroscopic measurements on nuclei beyond the proton drip line due to the hindrance of particle emission by the Coulomb and centrifugal barriers, allowing lifetimes ranging up to seconds. The uncharged neutron is not confined by the Coulomb barrier and so neutron emission occurs on timescales far shorter than proton emission, of the order 10^{-21} s.

The nuclei studied in this work are very close to, or beyond, the proton drip line.

2.3 Alpha Decay

The spontaneous emission of a helium ion from a nucleus is known as α decay, written as

$$^{A}_{Z}X_N \rightarrow ^{A-4}_{Z-2}Y_{N-2} + \alpha \tag{2.9}$$

where X and Y are the parent and daughter nucleus.

In nuclei of increasing proton number the Coulomb repulsion increases with

Z^2 in contrast to the nuclear force which increases approximately with A. Large nuclei therefore become increasingly susceptible to emission of charged particles. The α particle is the first doubly magic nucleus and is very tightly bound ($\approx$28 MeV) relative to nearby nuclei resulting in a large mass defect. The mass difference that drives nuclear decay is maximised when the decay products are tightly bound (resulting in a larger mass difference between parent and daughter) and so the α particle is favoured for particle emission when the Coulomb repulsion of a nucleus becomes significant.

From energy conservation

$$m_X c^2 = m_Y c^2 + T_Y + m_{He} c^2 + T_\alpha, \tag{2.10}$$

where m_X, m_Y and m_{He} are the atomic masses of the mother, daughter, and ^{4}He atoms respectively and T_Y and T_α are the kinetic energies of the daughter nucleus and α particle respectively.

The difference in mass is the energy available for the decay and is known as the Q-value

$$Q_\alpha = (m_X - m_Y - m_{He})c^2, \tag{2.11}$$

and from equations 2.10 and 2.11

$$Q_\alpha = T_\alpha + T_Y. \tag{2.12}$$

One can always choose a reference frame in which the mother nucleus is initially at rest and so from momentum conservation

$$P_\alpha = P_Y, \tag{2.13}$$

where P_α and P_Y are the momenta of the α particle and daughter nucleus

respectively.

In the non-relativistic regime (valid given $T \ll mc^2$) the kinetic energy can be written $T = \frac{p^2}{2m}$, and combining with equations 2.12 and 2.13 yields

$$T_\alpha \approx \frac{Q}{1 + \frac{4}{A_Y}}, \tag{2.14}$$

where 4 is the mass number of the α particle and A_Y is the mass number of the daughter nucleus. For the decay of an A=160 nucleus approximately 98% of the energy is carried away by the α particle.

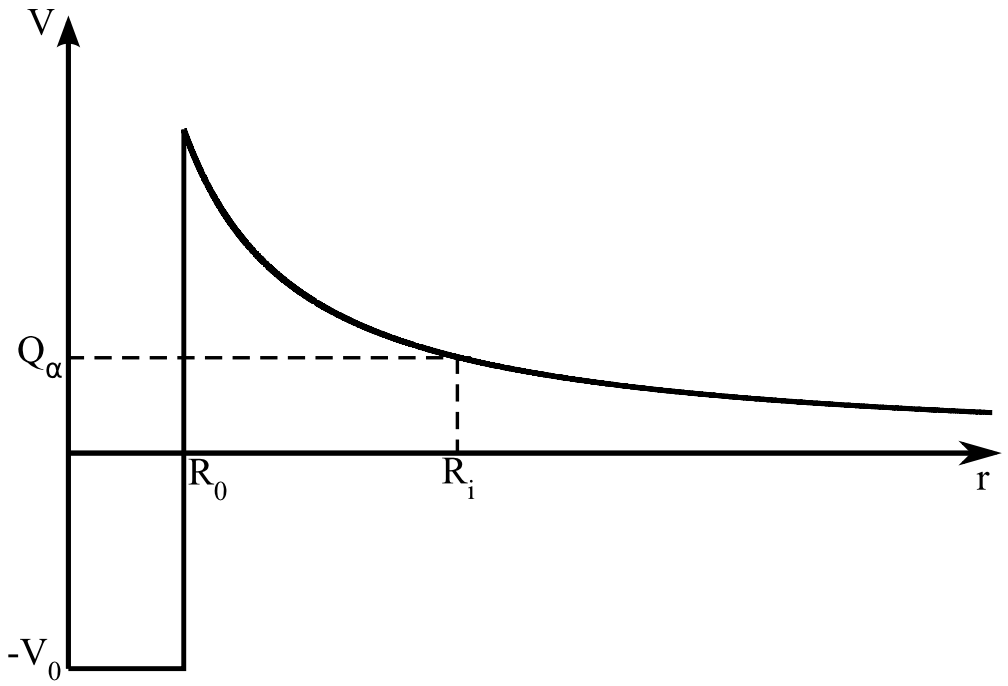

Figure 2.3: *Idealised potential of an α particle as a function of its separation from the mother nucleus.*

Theoretical approaches to α decay use one-body models in which the pre-formed α particle exists within the potential of the daughter nucleus. Figure 2.3 shows a simple, idealised potential of an α particle as a function of its distance from the daughter nucleus. It consists of a square well potential with depth $-V_0$ within the radius of the daughter nucleus, R_0, and a Coulomb

potential (and subsequent 1/r dependence) at larger radii.

A nucleus with a positive value of Q_α is prevented from immediate decay due to the presence of the Coulomb barrier. Classically, the α particle cannot enter the region where the potential is greater than the Q-value and α decay is forbidden. Quantum mechanically, however, there is some probability of the α particle tunnelling through the potential. At radius R_i the α particle has escaped the daughter nucleus and so $R_i - R_0$ is the distance which the α particle must penetrate.

The decay rate is given by

$$\lambda = f P_{tunnel} \tag{2.15}$$

where f is the frequency with which the α particle encounters the barrier and P_{tunnel} is the probability of tunnelling through the barrier. An approximate value of f is given by v/R_0 where v is the velocity of the α particle within the nucleus, obtained from its kinetic energy. P_{tunnel} is given by

$$P_{tunnel} = e^{-2G} \tag{2.16}$$

where G is the Gamow factor and represents the area through which the particle must tunnel. It is found using the WKB integral of the classically forbidden region [21] and is given by

$$G = \sqrt{\frac{2m}{\hbar^2}} \int_{R_0}^{R_i} (V(r) - Q)^{\frac{1}{2}} dr, \tag{2.17}$$

where m is the reduced mass of the α particle.

The potential shown in figure 2.3 is very simplistic, taking into account only a nuclear square well potential and an idealised Coulomb barrier. A more realistic model must account for the fact that a square well is not an accurate

representation of the nuclear potential (see section 2.1.2), that the Coulomb barrier is modified by the presence of atomic electrons and that there exists an angular momentum barrier dependent on the L values of the initial and final state. Rasmussen's work on α decay barrier penetrabilities uses a potential that is a sum of nuclear, Coulomb and angular momentum potentials [21] expressed as

$$V(r) = -1100\exp\left[-\left\{(\frac{r-1.17A^{1/3}}{0.574}\right\}\right]+l(l+1)\frac{\hbar^2}{2mr^2}+\frac{2Ze^2}{4\pi\epsilon_0 r}(MeV), \quad (2.18)$$

where Ze is the charge on the daughter nucleus and l is the angular momentum of the α particle.

Angular momentum and parity must be conserved in the decay, and a decay from initial state I_i^π to final state I_f^π is subject to the selection rules

$$\vec{l} = \vec{I_i} - \vec{I_f} \quad (2.19)$$

and

$$|I_i^\pi - I_f^\pi| \leq l \leq I_i^\pi + I_f^\pi. \quad (2.20)$$

The initial state with angular momentum L has parity given by

$$\pi_i = (-1)^L. \quad (2.21)$$

Whether the final state has the same or opposite parity to the initial state depends on the angular momentum, l, of the α particle:

$$\pi_f = \pi_i(-1)^l, \quad (2.22)$$

The one-body model of α decay assumes a preformed α particle which requires no rearrangement of nucleons before αdecay can occur. This may be interpreted as an αparticle existing within the spherical potential well of the daughter nucleus. Deviations between experimental and theoretical values indicate that a rearrangement of nucleons is required before α decay may occur and is a useful tool for deducing nuclear structure information. Larger values of l result in a greater hindrance of the decay, an effect which is in addition to the longer life time associated with an increased angular momentum barrier.

2.4 Proton Emission

Nuclei with a negative proton separation energy (see equation 2.7) are said to be proton unbound and may undergo proton emission, written

$$ {}^{A}_{Z}X \rightarrow {}^{A-1}_{Z-1}Y + p. \tag{2.23} $$

A nucleus may be proton unbound but Coulomb and angular momentum barriers hinder proton emission and result in lifetimes ranging up to seconds, allowing spectroscopic measurements to be made. The proton must tunnel through a classically forbidden region to escape the nucleus, and the theory of proton emission therefore follows a similar line to that of α decay: the tunnelling probabiltiy is given by the WKB integral of the forbidden region, given by equation 2.17 where $V(r)$ is a sum of nuclear, Coulomb and angular momentum potentials. The solution to this integral, i.e. the area through which the proton must tunnel is dependent on the Q-value and the height and width of the potential barrier. The Q-value is given by

$$ Q_p = (m_X - m_Y - m_H)c^2, \tag{2.24} $$

where m_H is the mass of a ^{1}H atom.

The Coulomb contribution to the potential barrier height is half that of α decay (ignoring the small screening effects of atomic electrons) while the contribution of the angular momentum potential is increased by a factor of four due to the inverse mass dependence seen in equation 2.18. The lifetime of proton-emitting states is therefore strongly dependent on the angular momentum, making proton emission a useful tool to investigate nuclear structure.

2.5 Beta Decay and Electron Capture

The term β decay refers to radioactive decay mediated by the weak force in which an electron or positron is emitted from the nucleus, or an electron is captured by the nucleus. β^- decay is the conversion of a neutron to a proton and emission of an electron and antineutrino and is written as

$$ {}^{A}_{Z}X_N \rightarrow {}^{A}_{Z+1}Y_{N-1} + e^- + \bar{\nu}. \tag{2.25} $$

β^+ decay is the inverse process, converting a proton to a neutron and emitting a positron and a neutrino, written as

$$ {}^{A}_{Z}X_N \rightarrow {}^{A}_{Z-1}Y_{N+1} + e^+ + \nu. \tag{2.26} $$

As before, the Q-value is equal to the total mass before and the total mass after the reaction. Neglecting the small difference in the final and initial electron binding energies the Q-values are written

$$ Q_{\beta^-} = (m_X - m_Y)c^2, \tag{2.27} $$

$$Q_{\beta^+} = (m_X - m_Y - 2m_e)c^2, \tag{2.28}$$

where the masses given are the neutral atomic masses. In converting from nuclear to atomic masses one must take into account both the mass of the atomic electron gained or lost, and the emitted electron or positron. In the case of β^- decay they cancel while in the case of β^+ decay they add, hence the discrepancy of $2m_e$.

The three body nature of β decay means that unlike α decay it is not a monoenergetic process. The electron or positron may be emitted with any energy from zero up to the Q-value of the decay, where the extreme cases correspond to the electron carrying away all or none of the decay energy. The form of the spectrum is shown in figure 2.4. From the Q-value and the known masses of initial and final products it can be inferred that the neutrino is massless to within the precision of the experimental masses.

Electron capture is a β-decay process which competes with β^+ decay and involves the capture of an electron by the nucleus and the subsequent conversion of a proton to a neutron, written as

$$^A_Z X_N + e^- \rightarrow {}^A_{Z-1}Y_{N+1} + \nu. \tag{2.29}$$

The Q-values given for β^- and β^+ decay assume a ground state to ground state process and the difference in binding energy is negligible. In the case of electron capture the final nucleus is necessarily in an excited state because there is a vacancy in the inner shell from which the electron has been captured. If it is captured from the nth shell with binding energy B_n, then the Q-value is given by

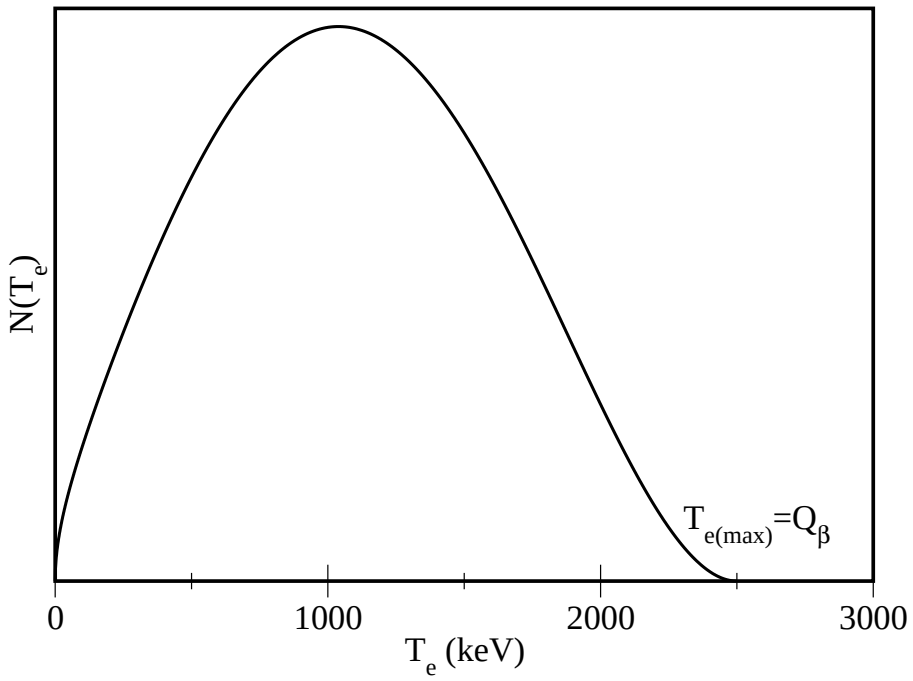

Figure 2.4: *Energy spectrum for electrons emitted in β^- decay with Q_β=2.5MeV.*

$$Q_\epsilon = m_X c^2 - m_Y c^2 - B_n. \tag{2.30}$$

From the expressions for Q_{β^-}, Q_{β^+} and Q_ϵ it can be seen that β^+ decay requires that the initial nucleus is more massive than the final nucleus by at least $2m_e$, while β^- decay and electron capture require only that the mass difference is as large as the difference in electronic binding energy. There are therefore cases where electron capture can occur but β^+ decay is forbidden.

2.6 Gamma Decay

γ decay is a process in which a nucleus de-excites via the emission of a high energy photon, written

$$ {}^{A}_{Z}X^{*} \rightarrow {}^{A}_{Z}X + \gamma \tag{2.31} $$

where the asterisk superscript denotes an excited state.

The properties of a γ-ray emission depend on the structure of the initial and final states of the nucleus from which it originated.

The energy of the recoiling nucleus is negligible for typical γ-ray energies, and so the energy of the the emitted photon, E_{γ}, is given by the difference in excitation energies of the initial and final state.

De-excitation of a nucleus is associated with a change in its electromagnetic field and the nature of the transition depends on the multipole of that field. A transition from initial sate I^{π}_{i} to final state I^{π}_{f} is subject to the selection rule

$$ |I^{\pi}_{i} - I^{\pi}_{f}| \leq L \leq I^{\pi}_{i} + I^{\pi}_{f}, \tag{2.32} $$

where L is the order of the multipole moment of the transition (1=dipole, 2=quadrople, 3=octopole etc), which also corresponds to the angular momentum carried by the emitted photon in units of $\hbar$. There is an exception to this selection rule which occurs when $I_f = I_i = 0$, which is that monopole transitions are forbidden since photons must have non-zero spin.

Parity changes for electric (EL) and magnetic (ML) multipoles are given by

$$ \Delta\pi(EL) = (-1)^{L} \tag{2.33} $$

$$\Delta\pi(ML) = (-1)^{L+1}, \tag{2.34}$$

meaning a parity change is associated with odd L for electric transitions and even L for magnetic transitions.

L	T_E (s)	T_M (s)
1	$6.73\ A^{-2/3}\ E_\gamma^{-3} \times 10^{-15}$	$2.24\ A^{0}\ E_\gamma^{-3} \times 10^{-14}$
2	$9.37\ A^{-4/3}\ E_\gamma^{-5} \times 10^{-9}$	$3.12\ A^{-2/3}\ E_\gamma^{-5} \times 10^{-8}$
3	$1.98\ A^{-2}\ E_\gamma^{-7} \times 10^{-2}$	$6.60\ A^{-4/3}\ E_\gamma^{-7} \times 10^{-2}$
4	$6.30\ A^{-8/3}\ E_\gamma^{-9} \times 10^{4}$	$2.10\ A^{-2}\ E_\gamma^{-9} \times 10^{5}$
5	$2.83\ A^{-10/3}\ E_\gamma^{-11} \times 10^{11}$	$9.43\ A^{-8/3}\ E_\gamma^{-11} \times 10^{11}$

Table 2.1: *Half-lives for electric and magnetic transitions with mass number A, and transition energy E_γ in MeV, based on Weisskopf estimates [22].*

In reference [23] Weisskopf estimates the transition probailities using a simplified model in which excited states are due to single-proton excitations moving independently within the nucleus. The half-lives predicted from these estimates can be found in table 2.1 for the lower order transitions. Weisskopf described the assumptions in this model as "extremely crude" and the estimates are most useful for giving the relative orders of magnitude for transitions of different multipole order rather than giving the absolute value for γ decay lifetimes. It can be seen from table 2.1 that lifetimes increase dramatically with increasing L. This allows other decay modes to dominate in the case where the only valid electromagnetic transition has a high multipolarity. Examples of this are described this work: ^{156}Hf and ^{158}W have α decaying 8^+ states due to the long lived nature of the E4 transitions required for γ decay in these nuclei. Similarly the $\frac{11}{2}^-$ state in ^{159}Re decays via proton emission because the fastest available γ decay is too long lived to compete.

Chapter 3

Experimental Apparatus

The majority of the nuclei that have been studied to date do not occur naturally and must be synthesised in the laboratory using an appropriate reaction type and beam and target combination. Having produced the nuclei of interest a number of detector types can be employed to measure their properties. The apparatus used to obtain the results in this work are described in this chapter while the techniques used to analyse the data are described in chapter 4.

3.1 Apparatus

The experiments described in this work were performed at the accelerator laboratory of the University of Jyväskylä. The K130 cyclotron was used to accelerate a beam of ionised ^{58}Ni nuclei to 318 MeV. The beam was incident on a stationary target of ^{106}Cd and nuclei of interest were synthesised in the subsequent fusion-evaporation reactions. Situated around the target position was the Light Ion Spectrometer Array (LISA) and JUROGAM II array. The reaction products were transported through the Recoiling Ion Transport Unit (RITU) to the focal plane and the GREAT spectrometer. The various com-

ponents of this set up are described in detail below.

3.1.1 JUROGAM II germanium array

Surrounding the target position is the Jurogam II detector array, a series of Compton suppressed hyperpure germanium (HP-Ge) detectors sensitive to γ-rays between 50 keV and 2 MeV emitted at the target position. The array is designed to detect the prompt γ rays that are emitted from the fusion-evaporation reaction. Chapter 6 shows spectra taken with Jurogam for the reaction product ^{159}Re.

The array consists of 15 'phase I' type [24] detectors (so called because they were used before the upgrade of JUROGAM) and 24 clover type [25] detectors. The former consists of a single crystal of germanium while the latter is segmented into four crystals. The clover detectors allow for higher efficiency due to the use of 'add-back' techniques, in which a photon which Compton scatters between crystals can have its full photopeak energy reconstructed by adding together the energy deposited in each crystal. For experiments such as this one in which LISA or other ancillary devices are employed the first ring of five phase 1 detectors is removed due spacial constraints.

The detectors have an entrance absorber to attenuate low energy photons and the entire array is cooled to 90K using liquid nitrogen to reduce noise from thermal excitations across the band gap. The Compton suppression is done using bismuth germanate (BGO) scintillators which surround each detector and are sensitive to photons that Compton scatter and fail to deposit all of their energy in the germanium.

3.1.2 LISA

The Light Ion Spectrometer Array (LISA) is an array of silicon detectors designed to detect charged particles at the target position.

The LISA detector system is a solution to the problem of studying exotic nuclei which do not have a sufficiently long life time to survive the flight time through the recoil separator (this value depends on the reaction used but is typically about 500 ns. In this work the flight time was 350 ns). It is designed to detect light charged particles (p, α) emitted promptly from short lived states of the recoils, but in this work was utilised for channel selection of ^{160}Os, produced through a pure neutron channel, by vetoing all events that are coincident with charged particles emitted at the target position. This technique is described in detail in chapter 4.

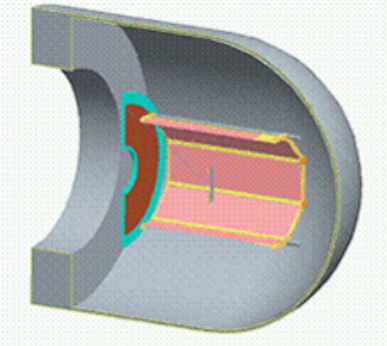

Figure 3.1: *Schematic of LISA inside the target chamber showing both the annular and barrel detectors, taken from reference [26].*

Eight silicon detectors, each with four strips along the beam axis, form a barrel around the target position, while eight more silicon detectors form an outer layer to the barrel, allowing particle identification using a ΔE-E technique. An annular double sided silicon strip detector, with 64 radial strips and 32 annular strips, lies downstream of the barrel detector.

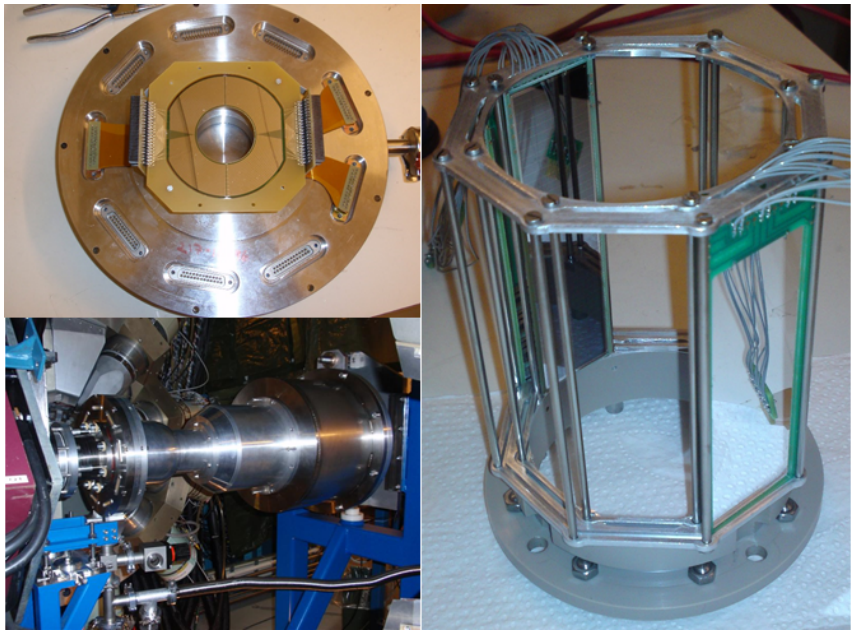

Figure 3.2: *Right and top left: photographs of the LISA barrel and annular detectors under construction. Bottom left: photograph taken during the installation of LISA at the centre of JUROGAM. Photos taken from reference [27].*

3.1.3 RITU

The spectroscopic results described in chapters 5 and 6 rely on the ability to identify the reaction products in which we are interested and discriminate them from the large number of background events. Only a small percentage of the beam reacts with the target and the first step in the process of identification is to separate reaction products leaving the target position from unreacted beam, a task for which the Recoiling Ion Transport Unit (RITU) is used. RITU has a QDQQ configuration, where Q refers to a quadrupole magnet and D is a dipole magnet. Together these magnets act to focus and bend the beam such that the reaction products are transmitted to the GREAT spectrometer with the greatest possible efficiency while the unreacted beam is dumped.

A particle with charge eq moving perpendicular at velocity $\vec{v}$ to a magnetic field of strength $\vec{B}$ experiences a force $\vec{F}$ according to

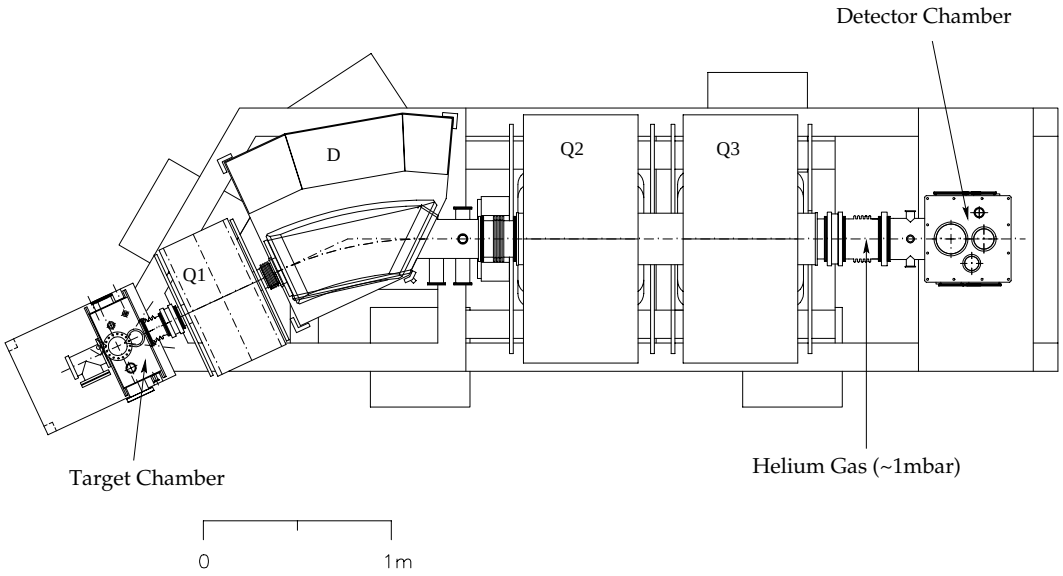

Figure 3.3: *The gas filled separator RITU, taken from reference [28].*

$$\vec{F} = eq\vec{v} \times \vec{B} \tag{3.1}$$

By equating this to the force required to accelerate a body around a circle of radius r and substituting $Z - N_e$ for the charge on an ion where Z is the atomic number and N_e is the number of missing electrons, it can be shown that

$$r\vec{B} = \frac{uA\vec{v}}{e(Z - N_e)} \tag{3.2}$$

where uA is the mass of the ion. The mass to charge ratio ($\frac{A}{Z-N_e}$) therefore defines the bending radius in the separator and recoils, fission fragments and scattered beam may be effectively separated provided this value is sufficiently different for each. In vacuum mode separators the recoils are in a known charge state and the different bending radii allows for an unambiguous mass assignment to be given to the recoils. In a gas-filled separator such as RITU the recoils exchange electrons through multiple interactions with the atoms

of the helium gas. The result is a distribution of averaged charge states, in which any one recoil will have a charge state which fluctuates about the mean. This significantly decreases the range of the angular distribution of the recoils and, given the limited angular acceptance of RITU, increases the transport efficiency of the separator. However this comes at the cost of a degraded mass resolution.

3.1.4 The GREAT spectrometer

The GREAT detector array [29] (Gamma, Recoil, Electron, Alpha, Tagging), located at the focal plane of RITU, consists of a number of detectors and is designed to measure the radioactive properties of the products transported through the separator.

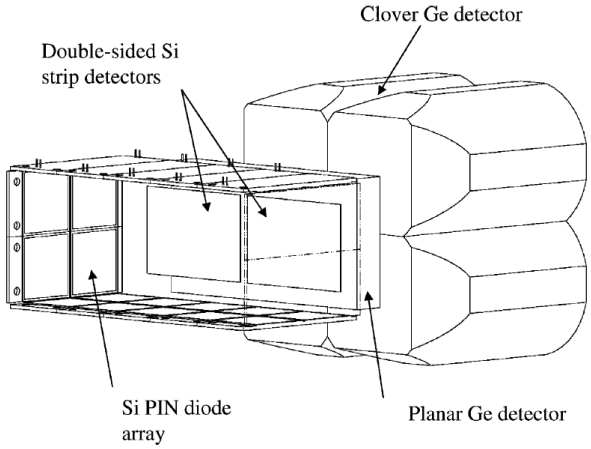

Figure 3.4: *The GREAT spectrometer. Taken from reference [29].*

Multi-wire proportional counter

Located at the entrance to GREAT is the multi-wire proportional counter (MWPC) with dimensions of 131mm × 50mm, containing isobutane, through

which reaction products pass before being implanted in the DSSDs. The MWPC is used in conjuction with the DSSD to identify whether signals seen in the DSSD originate from the implantation of a reaction product or from the decay of an ion that has already been implanted, and is therefore integral to identifying the correlations that isolate the nuclei of interest in this work. Section 4.2 gives further detail on how the MWPC is used in particle discrimination. Thin Mylar foil entrance and exit windows separate the isobutane from the low pressure helium of RITU and the vacuum of GREAT. Energetic particles ionise the isobutane producing free ions and electrons, which are accelerated by an array of high voltage wires creating a cascade of further ionisation. The charge carriers are collected by the wires, and the total charge collected is proportional to the energy of the initial ionisation.

DSSD

At the heart of GREAT is a pair of double sided silicon strip detectors (DSSDs) mounted side by side. The DSSDs function both to detect implantions of reaction products after they pass through the MWPC and to measure their subsequent charged particle decays and it is primarily from the DSSD that the spectroscopic information outlined in the results chapters of this work is collected. Pixels are formed from the cross hatching of vertical and horizontal strips. It is the correlation within a single pixel of an ion implantation with its subsequent decays that is the basis for identifying which species of nucleus has been implanted. Each DSSD has a thickness of 300 μm. The active area is 60 x 40 mm with a strip pitch of 1 mm giving 4800 individual pixels. Ethanol is circulated through the cooling block to cool the DSSDs to -20°C to reduce the noise contribution from thermal excitations. Reaction products are implanted into a DSSD pixel at a depth of 1-10 μm. This compares with a typical range

of charged particle decays through silicon of 20-50 μm, resulting in a significant probability of escape without full energy deposition.

PIN diodes

An array of 28 silicon PIN diodes is located upstream from the DSSDs. The primary function of these diodes is to detect conversion electrons, which have a significant probability of emerging from the DSSDs given the relatively low implantion depth of the recoils. A secondary function of the PIN diodes, and their use in this work, is to detect escaped α decays. This may be used as a veto to reduce the spectrum of escaped alphas, or to increase statistics by summing together the energy deposited in the DSSDs and the PIN diodes to regain the full energy deposition, although this technique results in degraded energy resolution.

3.2 Total Data Readout (TDR)

Readouts from all detectors are recorded using a triggerless Total Data Readout (TDR) acquisition system [30], and time stamped with a precision of 10 ns using a global 10 MHz clock. Prior to the installation of the TDR set up only data that passed a hardware trigger would be recorded, which results in all detectors being limited by the dead time of the trigger detector, referred to as 'common dead time'. The elimination of common dead time is particularly important for establising correlations in the DSSD since it prevents each strip from being limited by the dead time occurring due to a pulse in a different strip. The use of a triggerless data readout, in which all data are recorded and particles are discriminated at a software level rather than a hardware level, allows for greater flexibility in the analysis stage. In this work the precision of

the TDR (10 ns) was typically much smaller than the error from low statistics when measuring the half-life of decays, and small also compared to the correlation times used and the dead time of strips in the DSSD. Analysis of the data was done using the Java-based Grain software package [31].

Chapter 4

Experimental Methods

4.1 Fusion-evaporation reactions

With increasing nuclear mass more neutrons are required to bind the nucleus together against the repulsive electrostatic force of the protons, and the line of stability quickly falls below the N=Z line. A fusion of two nuclei therefore produces a compound nucleus on the neutron deficient side of the chart, which makes fusion-evaporation reactions suitable for studies of highly neutron deficient nuclei.

After the collision a compound nucleus is formed within about 10^{-21}s and is left in a highly excited state ($\approx$ 50 MeV). Offsets between the centres of mass of the incoming and target nuclei result in a large excess of angular momentum ($\approx$30 $\hbar$) and a high probability of fission. If the nucleus remains intact then particle evaporations will carry away excess energy at approximately 6-10 MeV per particle on a time scale of the order of 10^{-19} s. The number and type of particle evaporations is highly dependent on the beam energy, which is chosen to give the highest possible probability of the desired exit channel. However, it remains a probabilistic process and many different evaporation residues ('re-

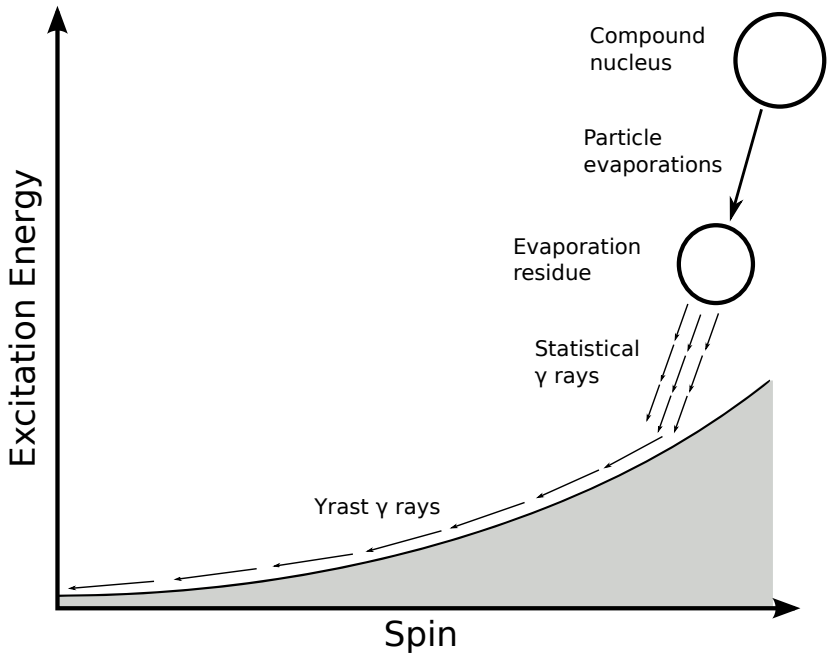

Figure 4.1: *The mechanisms through which the compound nucleus de-excites during a fusion evaporation reaction.*

coils') will result from any given reaction and beam energy combination.

As the excitation energy decreases γ decay becomes a competing decay mode and quickly dominates over particle evaporation. Initially the density of states is very high and the γ rays are statistical in nature (i.e. they cannot be resolved). These statistical γ rays are dipole transitions, they occur on a timescale of about 10^{-15} s and carry the nucleus into the yrast region, as shown in figure 4.1. The yrast line typically de-excites via quadruple transitions which are slower (10^{-11} s) and less energetic. These cascades of yrast γ rays can be resolved and will yield useful nuclear structure information. If the de-excitation hits an isomeric state then any subsequent transitions will be delayed and may not occur in the target chamber. Ideally they will be delayed sufficiently to be detected at the separator focal plane, However in the case that they do not last long enough to survive the flight time through RITU (approximately 400

ns in this work) they will occur whilst the nucleus is in transit and cannot be detected.

4.2 Particle discrimination

When a signal is detected in the DSSDs the first step before meaningful information can be extracted is to identify what manner of particle it is. Recoils can be discriminated from decay products by an energy loss signal in the MWPC (through which the recoils pass but decay products do not). However, fission products and scattered beam also deposit energy in the MWPC and more sophisticated techniques must be used to properly identify recoils: A 2D matrix of energy loss in the MWCP against flight time between the MWPC and DSSD produces a characteristic signal that allows recoils to be distinguished from background, as shown in figure 4.2.

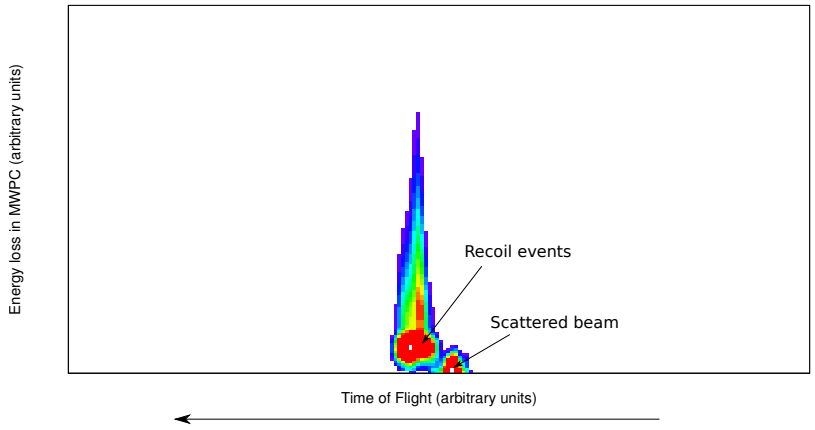

Figure 4.2: *Energy loss in the MWPC against flight time between the MWPC and the DSSDs. Recoil events can be distinguished from scattered beam.*

Decay events are identifed by a DSSD signal that is not coincident with a MWPC energy loss signal and has been preceded by a recoil implantion in the same pixel. Further decay events (necessary, for example, when trying to

establish a recoil-mother-daughter correlation) must occur in sequence in the same DSSD pixel.

Useful γ rays at the target position are identified by an energy deposition in JUROGAM that can be temporally correlated with a recoil implantion in the DSSDs (i.e. the time separation matches the flight time through RITU). A 2D matrix of recoil-γ time against recoil time of flight allows for the selection of only those γ rays that have the correct time separation from the recoil implantion to account for the flight time through RITU (see figure 4.3). In most cases it is necessary to know which nucleus the γ rays originate from, and so an additional condition is added requiring that the recoil can be identified by its subsequent decay in the DSSD. This is known as recoil decay tagging (RDT). If the nucleus is produced with a low cross section compared to other nuclei in the reaction it may be necessary to require a further decay (i.e. a recoil-mother-daughter correlation) for unambigious selection. This is the case for the γ-ray spectrum found for ^{159}Re in chapter 6.

4.3 Calibrations

All spectroscopic measurements rely on on the conversion of the electronic output from a detector to the corresponding measurement. There are many subtle factors that occur at the hardware level that will affect the electronic output, and so before any experimental analysis can be performed it is necessary to properly calibrate all detectors using known radioactive sources. The calibration is performed at the software level. An external calibration refers to the case where a stationary source is placed in the detector, while an internal calibration is performed using the decays of known reaction products.

In this work a quadratic fit was used to calibrate Jurogam using ^{152}Eu and

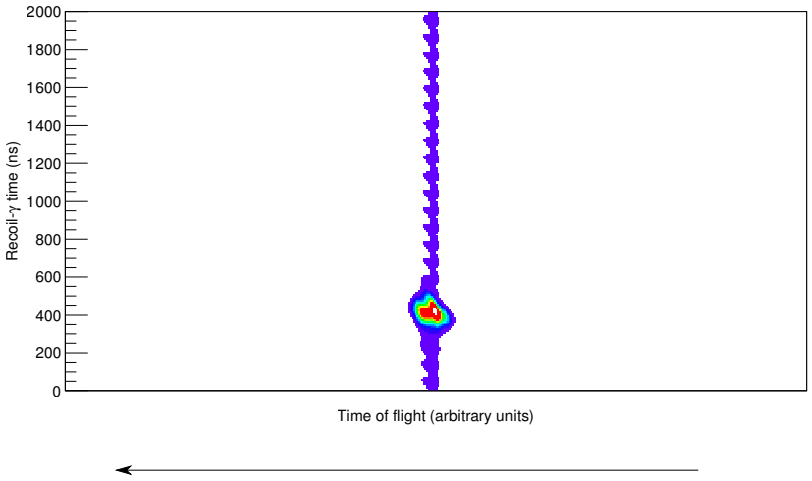

Figure 4.3: *Recoil-γ time against flight time of the recoil between the MWPC and DSSDs. The bright spot at around 400ns corresponds to the high density of γ rays correlated with a recoil. It contains two components due to small timing discrepancies (of the order of ns) between the two DSSDs due to small differences in the time it takes the electronics to process the signal. The long tail is background, with the periodic structure corresponding to the cyclotron frequency.*

^{133}Ba sources which undergo β decay to excited states in ^{152}Sm and ^{152}Gd which then de-excite through via known γ transitions ranging in energy from 80 keV to 1408 keV.

An external calibration is unsuitable for the DSSDs due to the energy loss through the dead layer which occurs for decays that are emitted externally but not for the decays of an ion which is implanted within the active area of the detector. The silicon detector also has a different response to αs than it does to protons, and each requires its own calibration. Proton decays emanating from ^{156}Ta, ^{160}Re and ^{161}Re were used for the internal proton calibration and the α decays of ^{150}Dy, ^{152}Er, ^{158}Ta, ^{156m}Hf and ^{156m2}Lu were used for the α calibration, using a linear fit.

In this work it was necessary to apply a correction to the DSSD calibration. The energetic nature of a recoil implantation results in a voltage pulse that is

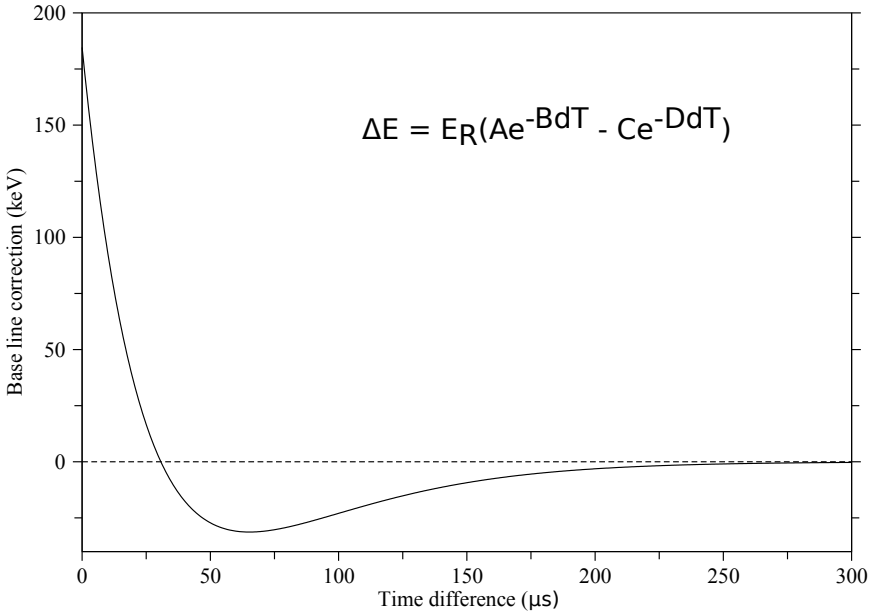

Figure 4.4: *An example of base line correction required due to a recent high energy implantation. E_R is the energy of the previous recoil, dT is the time since the previous recoil, and A, B, C and D are empirical constants. In this example E_R = 12 MeV, and A=159.446, B=0.0306467, C=144.062, and D=0.0273434.*

higher than normal and therefore takes longer than usual to decay away, and then overshoots the baseline, before returning to zero. Decays which occur in this time period will register an erroneous energy and must be 'base line corrected'. The base line correction is a function of the preamplifier and the empirical constants used to fit the correction must be calibrated individually for each strip of the detector. The function used is given in figure 4.4 along with an example correction applied to one of the strips.

4.4 Doppler-Shift correction

A photon emitted from a moving source will be doppler shifted when measured by a stationary observer. This energy shift can be accounted for by applying a correction during the data analysis stage but will still result in a degraded resolution.

When a moving recoil emits a γ-ray which is subsequently detected by a stationary detector the measured energy of the photon will be Doppler shifted according to the equation

$$E' = E\frac{\sqrt{1-\beta^2}}{1-\beta cos\theta}, \tag{4.1}$$

where E' is the measured energy, E is the energy in the rest frame of the recoil, β is the velocity as a fraction of the speed of light and θ is the angle at which the photon is emitted relative to the path of the recoil.

A first order approximation in the limit of $v \ll c$ is

$$E' = E(1+\beta cos\theta). \tag{4.2}$$

Given that the lifetime of excited states is very short compared to the time it takes a recoil to traverse the target chamber it is assumed that the photon is emitted from the target position and θ is taken to be the azimuthal angle of the detector. The mean velocity of the recoils can be calculated by measuring the energy shift of known transitions. In this work the target position was changed during the experiment from the centre of the target chamber to the entrance. It was therefore necessary to calibrate for two different values of θ at the analysis stage.

There is some variation in both the magnitude and direction of the recoil velocity, while the finite size of the detector means there is variation in the angle

at which the photon enters the detector. Additionally, photons emitted from long lived states or any states fed by a long lived state may be emitted some distance from the target position resulting in further variation of the angle. These factors result in a 'smearing' of the corrected energy and a degraded energy resolution known as Doppler broadening.

4.5 Background Suppression with the PIN Diodes

The implantation depth of a recoil in the DSSD is about 1-10 μm [29] while the range of a 5 MeV α particle through silicon is approximately 25 μm. There is therefore a significant chance that an α decay will escape the DSSD, leaving only a portion of its energy behind. This creates two potential problems: firstly that the nucleus can no longer be correctly identified by the DSSD energy signal, and secondly that the portion of energy which is deposited may match that of a lower energy α decay resulting in an incorrect assignment. However, the α particle may enter the PIN diodes (with a geometrical efficiency of about 30 % for particles emitted in the backwards hemisphere relative to implantation) and deposit the remnant of its energy there. This may be used as a veto condition to remove events involving escaped α decays to remove any possibility of a false assignment, or in some cases it is possible to reconstruct the full energy deposition and reclaim the event. This technique is hampered by the poor energy resolution of the PINS compared to the DSSDs.

Figure 4.5 shows the effect of a PIN veto on a DSSD energy spectrum, overlaid in red with the same spectrum with a PIN veto applied. The activity between the upper end of the spectrum of β decays and the lower end of the region of distinct α decays (i.e. about 0.8 - 4 MeV) is mostly escaped α decays, which is significantly decreased after the veto. The region below this

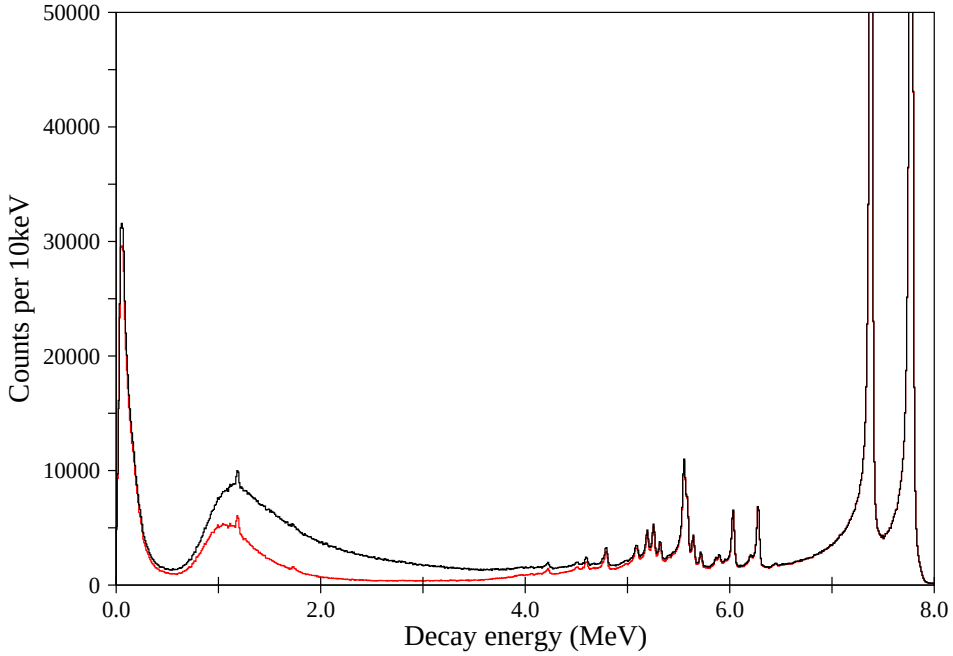

Figure 4.5: *Spectrum of decays occurring within 1 ms of a recoil implantation (black) compared with the same spectrum after all events that are in coincidence with activity in the PIN diodes has been vetoed (red).*

is primarily β decays: only a small proportion of the events in this region are due to the escape of either either α or β particles, which is why the PIN veto causes less suppression in this region.

An example of using the PIN diodes to reduce background for a given mother daughter correlation is shown in figure 4.6. This figure shows the α decays that are preceded by the proton decay of ^{160}Re selected to emphasise the ^{160}Re proton - ^{159}W α decay correlation (specifically, three times the half life for each correlation). The ^{159}W α decay is clearly seen at 6290 keV. The black line is before a PIN veto is applied, the red line shows the effect of applying the veto to both mother and daugher decays. The number of counts

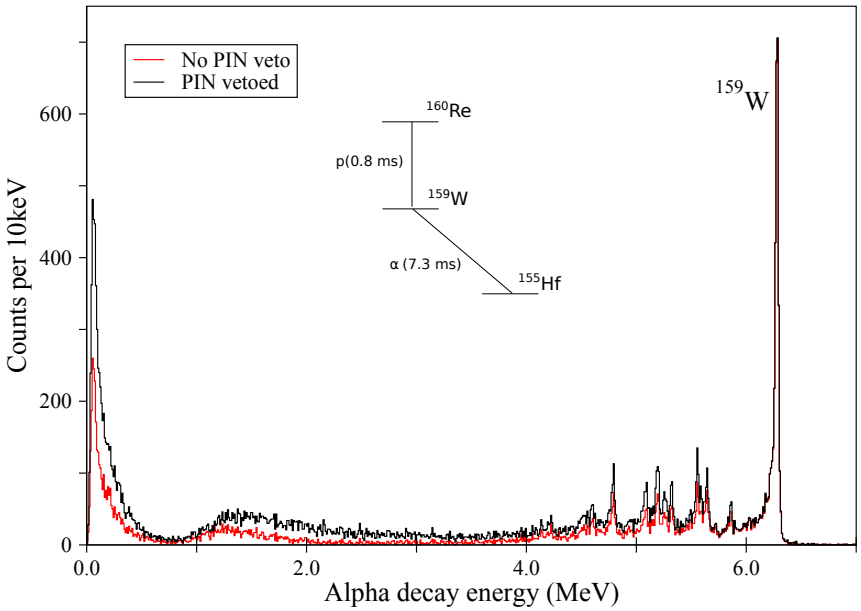

Figure 4.6: *Spectra showing the α decay of ^{159}W correlated with the proton decay of ^{160}Re both before (black) and after (red) a PIN veto is applied to both mother and daughter decays.*

below the ^{159}W peak is reduced by approximately a factor of two as the PIN veto suppresses the effects of escaped α decays.

In some cases it is possible to reclaim events lost to escaped α decays by adding together the energy deposited in the DSSDs and the PIN diodes. Figure 4.7 shows the sum of the energy seen in the DSSDs and the PIN diodes for events preceding a ^{158}W α decay. The dominant peak is the ^{159}Re proton decay and emerges in this spectrum for the case where there is no PIN diode activity. The activity above this peak are reclaimed α decays, where some energy has been deposited in the PIN diodes and added to the energy deposited in the DSSDs. The sum is greater than the correct decay energy due to the calibration method incorrectly accounting for the energy loss of α particles through the

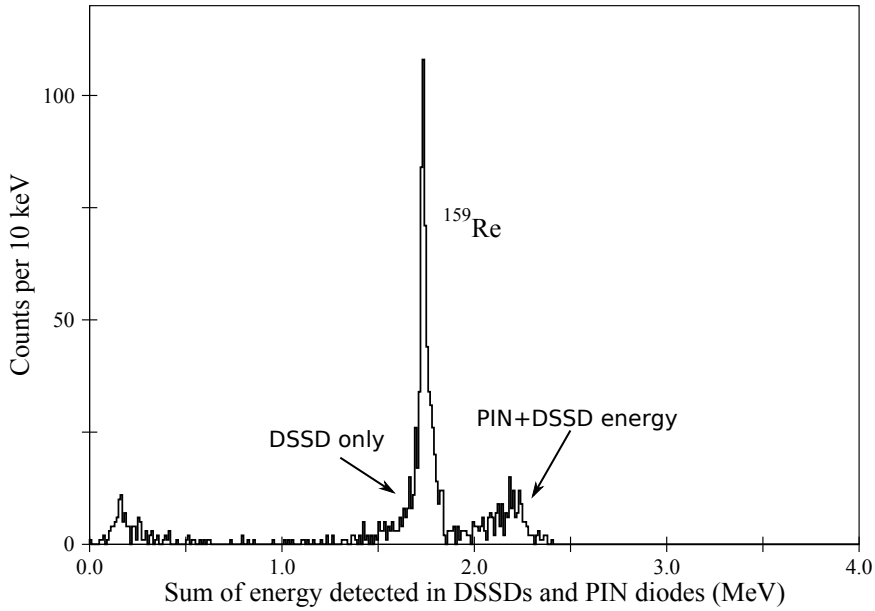

Figure 4.7: *Energy spectrum showing the sum of the energies deposited in the DSSDs and the PIN diodes for events preceding a* ^{158}W α *decay. The main peak is due to events where the full energy is deposited in the DSSDs while the activity above the peak is due to events where the energy is split between the DSSDs and the PINs.*

dead layer, which varies as a function of angle. This is not an issue when no spectroscopic information is being obtained from the energy and it is sufficient to simply establish that a recoil-mother-daughter correlation occurred, as is the case where this technique has been used in chapter 6.

Figures 4.8a and 4.8b show the DSSD events that occur within 4 ms of the main ^{159}Re peak and the high energy activity respectively. The fact that the ^{158}W α decay emerges clearly in both cases confirms that the PIN add-back is working as expected. In this example the number of recoil-mother-daughter correlations has been increased by about 40% with the use of a PIN addback technique for the mother correlation. This can be increased further by applying

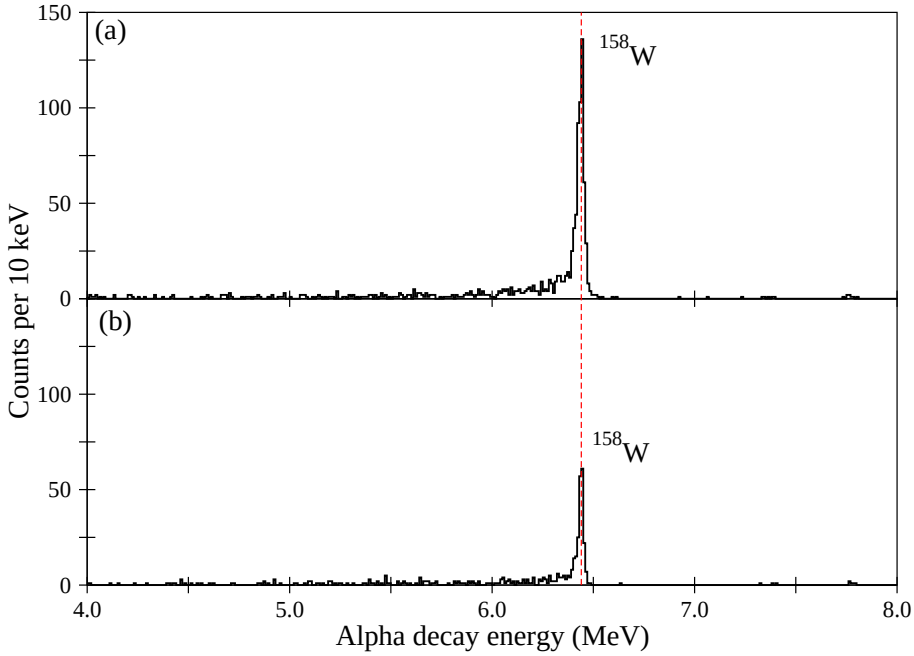

Figure 4.8: *(a)DSSD Energy spectrum for events occurring within 4ms of the main ^{159}Re peak shown in figure 4.7. (b) As (a) but with the mother energy gate set around the acitivty above the main peak.*

to the daughter correlation also, as has been done when collecting the γ ray spectrum in chapter 6.

4.6 LISA as a channel selector

The primary purpose of LISA is to perform charged particle spectroscopy of nuclei that are too short lived to survive the flight time to GREAT, but a secondary use is as a channel selector. The initial mode of de-excitation for nuclei formed in fusion reactions (assuming that they do not immediately fission) is particle evaporation. The evaporation particles may be neutrons, protons or α particles and the latter two can be detected in LISA. In this work

no attempt was made to differentiate α evaporations from proton evaporations.

In principle LISA may be used to select those recoil events that are associated with the correct number of charged particle evaporations for the desired exit channel. However, given an N charged particle exit channel with LISA operating at detection efficiency ϵ the probability, p, of detecting all charged particle evaporations is given approximately by

$$p \approx \epsilon^N \tag{4.3}$$

This probability drops off further when one considers that multiple charged particles cannot be seen in the same detector due to dead time. With LISA operating at $\epsilon \ll 100\%$ one has a low probability of detecting all N charged particle evaporations and a high probability of mis-assigning high N events as lower N events. LISA is therefore an ineffective channel selector for multiple charged particle exit channels.

However for neutron-only evaporation channels, such as ^{160}Os in this work, LISA can still be effective as a channel selector. In this case one can require that an event is not coincident with any charged particle detected in LISA, and the probability, p_{veto}, of suppressing a background event that has N charged particle evaporations is given approximately by

$$p_{veto} \approx 1 - (1 - \epsilon)^N \tag{4.4}$$

Figure 4.9 [33] shows the background-to-signal ratio when LISA is used as a channel selector as a function of LISA efficiency, as compared to the background-to-signal ratio without channel selection. In this experiment the efficiency of LISA was sub-optimal due to a number of detectors not working. At this operating efficiency the ratio degrades for all channels except $N = 0$

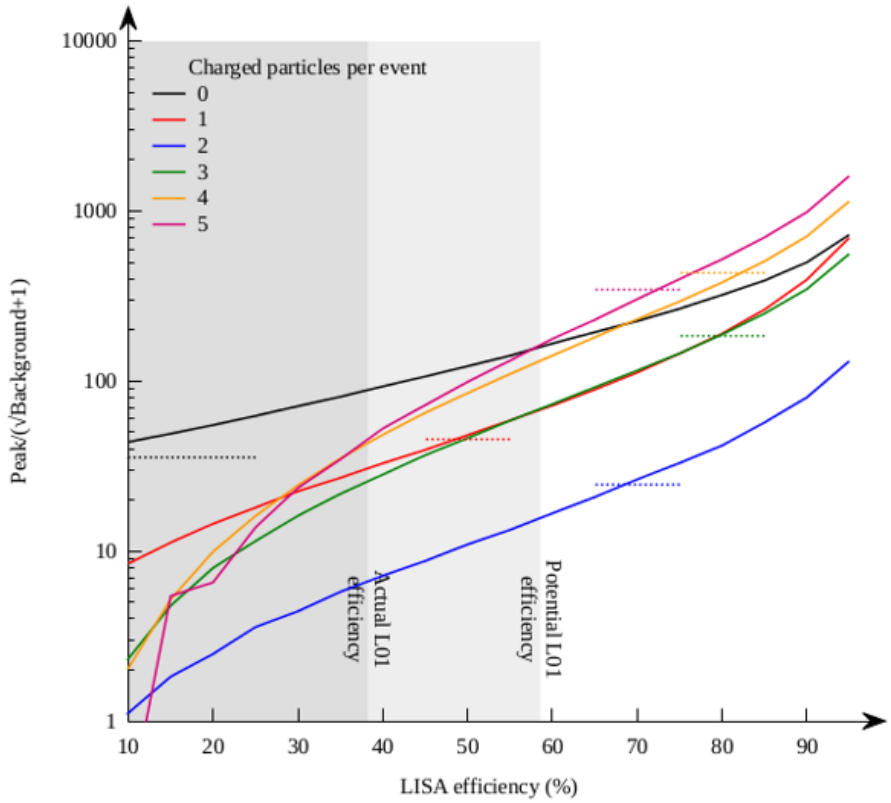

Figure 4.9: *Ability to select charged particle evaporation channels using LISA (solid lines) compared with no channel selection (dotted lines) Evaporated particle distribution for this reaction was simulated using PACE4 [32]. This image is reproduced from Ref. [33].*

when using LISA as a channel selector. At optimal efficiency LISA may also be an effective channel selector for $N = 1$.

^{159}Re and ^{155}Lu were both produced in the reaction. ^{159}Re was produced in a p4n (N=1) channel and ^{155}Lu is produced through either a p2α (N=3) channel or a 3p2nα channel (N=4). Figure 4.10 shows the effect on the number of these events when a LISA veto is applied. ^{159}Re is suppressed by 37% while ^{155}Lu is suppressed by 75%. From equation 4.4 this corresponds to an efficiency for detection of charged evaporation particles of around 35% (37% for the ^{159}Re measurement and between 30% and 37% for the ^{155}Lu measurement, depending

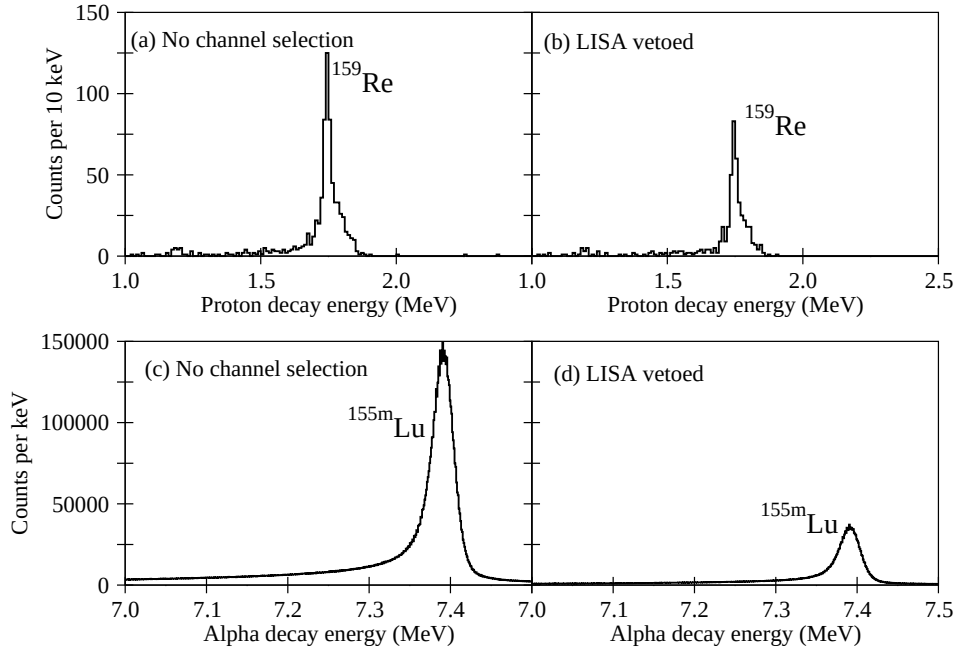

Figure 4.10: *(a) and (b) show the effect of using a LISA veto on* ^{159}*Re, produced in a one charged particle channel. (c) and (d) show the effect on* ^{155}*Lu, which may be produced in a three or a four charged particle channel.*

on which channel dominates).

Chapter 5

Evidence for the alpha decay of ^{160}Os

In this chapter evidence for the first observation of α decay from the ground state of the previously unseen isotope ^{160}Os is presented.

As described in chapter 1 ^{160}Os is expected to have an α-decaying 0^+ ground state and 8^+ isomeric state, but there is also the possibility that the isomer may decay by two-proton emission. A search for the isomeric state must therefore include both alpha and two-proton emitting possibilities. Observation of two-proton emission would make ^{160}Os the heaviest of a very small number of nuclides that have been observed to undergo this exotic decay mode.

5.1 Results

This work utilised fusion-evaporation reactions at the University of Jyväskylä accelerator laboratory. Details on the experimental apparatus may be found in chapter 3. A beam of ^{58}Ni was incident at 318 MeV on a 1mg/cm^2 ^{106}Cd target. Charged particles were detected in the DSSDs, and recoils and particle

decays were identified with the techniques outlined in chapter 4 using the MWPC, TAC measurements, and DSSD signals. The PIN diodes were used to suppress the background occurring due to decays that did not deposit their full energy. The proposed α decay was found using recoil-mother-daughter correlations and has an energy of 7230 keV. The expected 8^+ isomeric state has not been observed.

Two more data sets were analysed to search for further evidence of ^{160}Os. These experiments were performed at lower beam energies and intensities, and without the LISA spectrometer. These differences aside, they had the same experimental set up. No evidence of either the ground or isomeric state of ^{160}Os was found in these data sets. The experiments (denoted by the codes by which they may be identified in the records of the University of Jyväskylä) are summarised in table 5.1.

Table 5.1: Summary of experiments analysed.

Experiment	Beam energy (MeV)	Intensity (pnA)	Period (hours)	^{160}Os evidence
(a)L01	318	6.4	292	yes
(b)R31	300	4.7	75	
	290	2.3	104	none
(c)JR69	310	3	100	none

The lack of evidence of ^{160}Os in experiments (b) and (c) may be explained by to the fact that experiment (a) had the greatest duration and intensity, giving it a much higher probability of producing statistically significant numbers of ^{160}Os nuclei. Furthermore, even if ^{160}Os was produced in experiments (b) and (c) the absence of a target position detector capable of providing channel selection (such as LISA) would make it difficult to isolate this signal. It is unclear which experiment had a beam energy which is closest to optimal for producing ^{160}Os . Figure 5.1 shows the excitation functions for nu-

clides produced in a ^{58}Ni + ^{106}Cd reaction calculated using PACE [32]. While

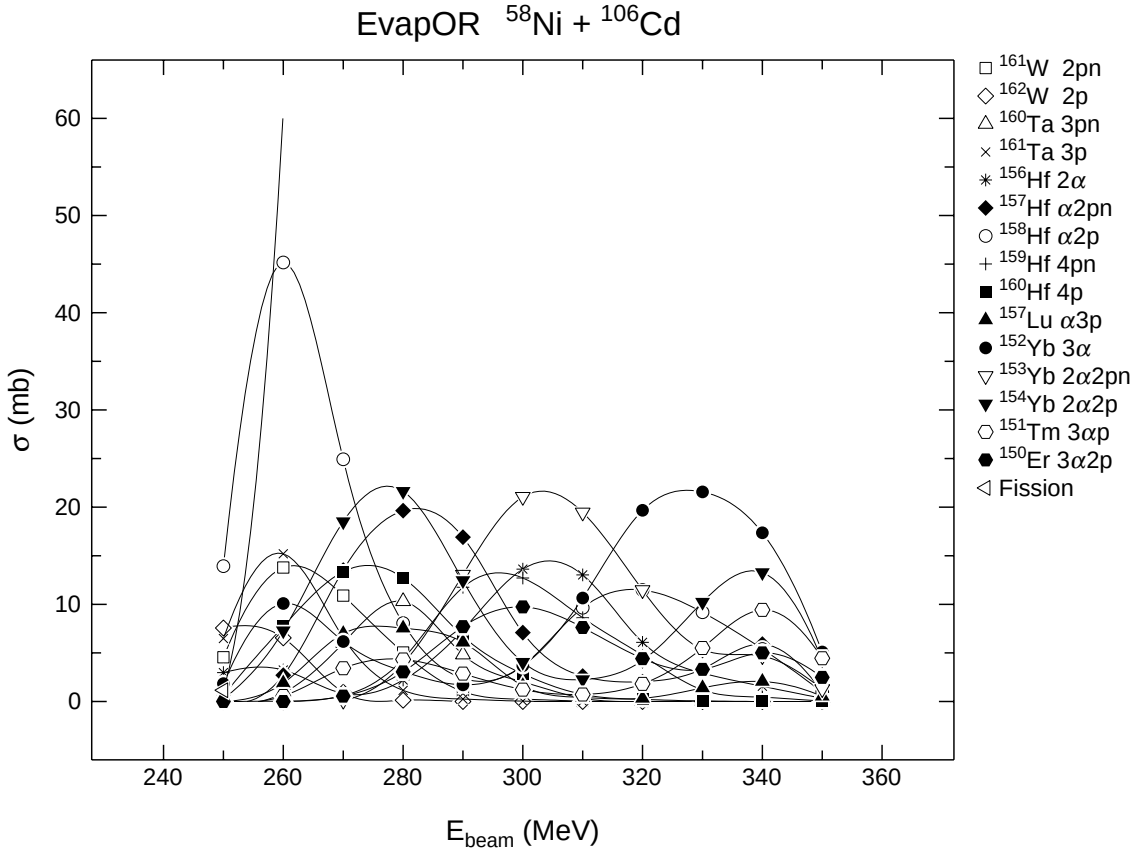

Figure 5.1: *Excitation functions for nuclides produced in a ^{58}Ni + ^{106}Cd reaction [32].*

these calculations are known to be unreliable for absolute cross sections of weak channels the value of the excitation function peak energy should still be reasonably accurate. Reference [34] found that the optimal beam energy to produce a proton-rich isobar through an *xn* channel is very similar to that of less exotic isobars through the evaporation of the same number of particles. Therefore the optimum beam energy for ^{160}Hf or ^{160}Ta (both produced in four-particle evaporation channels) from figure 5.1 could give an indication of the ideal beam energy for producing ^{160}Os in the same reaction. Given an energy loss of approximately 15 MeV/mgcm^{-2} and a target thickness of 1 mgcm^{-2}

the optimum energy might be expected to be approximately 295 MeV. It is possible that in this highly neutron-deficient region pure neutron channels require a higher beam energy, although this would not be consistent with the findings of reference [34] which found an approximate symmetry between the optimum beam energy for pn and $2n$ channels in the neutron deficient region above ^{100}Sn.

^{160}Os nuclei created though a four neutron evaporation channel would undergo the decays shown in figure 5.2. ^{160}Re and ^{160}W were also populated in this reaction, with a greater cross section than ^{160}Os, and decayed to the ground states of ^{156}Ta and ^{156}Hf, respectively.

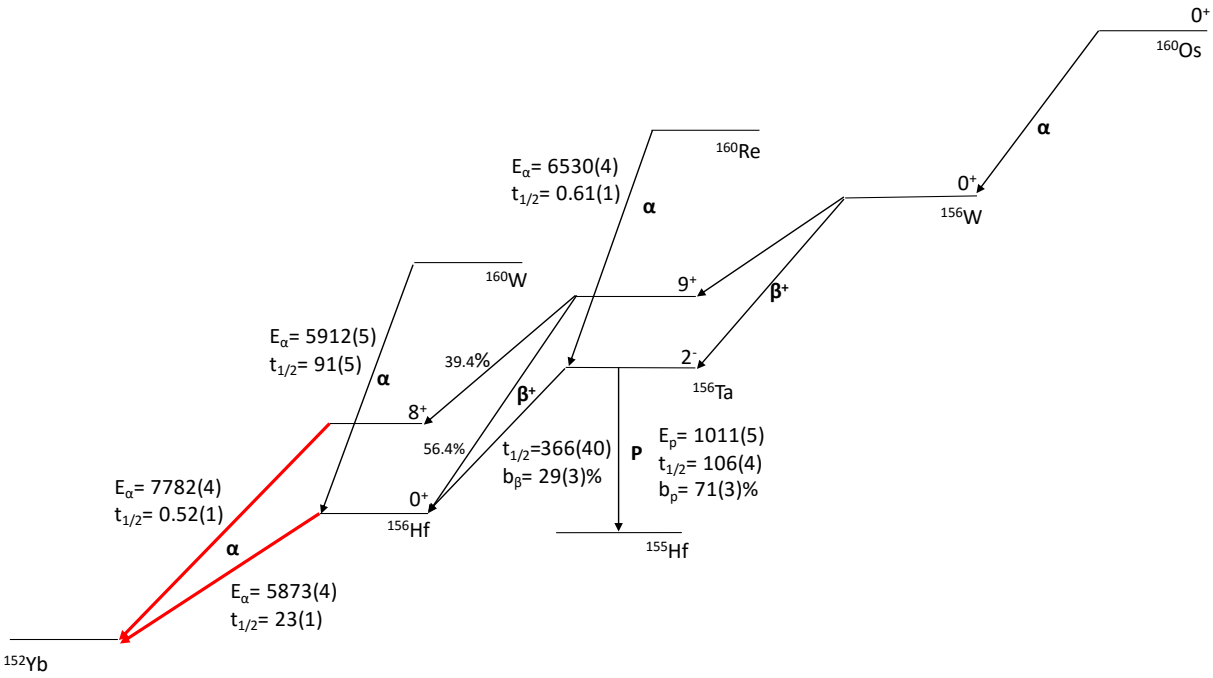

Figure 5.2: *Decay scheme of ^{160}Os. Decay energies (in keV), half-lives (in ms) and spins and parities are taken from references [14] and [35]. The energies given here are the decay energies instead of the Q-values because they are the observable values used in the analysis. The correlations used to search for ^{160}Os are highlighted in bold red. See text for discussion.*

Identification of ^{160}Os amongst the large number of events was achieved

using recoil-mother-daughter correlations. β decays are not mono-energetic due to the three body nature of the decay, and so it is not possible to identify the mother nucleus uniquely from measuring the decay energy. This, combined with the low detection efficiency for positrons and the competing process of electron capture, makes β decays unsuitable for mother-daughter correlations. At first sight the proton-emitting ground state of ^{156}Ta, with a branching ratio of 71% and half-life of 106 ms, looks like a promising candidate to use as a correlation. However, it was found to introduce a large amount of background due to its location in the spectrum of escaped alphas: the effect of using this correlation is discussed in greater detail in section 5.1.6. Instead, The α-emitting ground state and isomeric state of ^{156}Hf, which are highlighted in figure 5.2, were used to identify ^{160}Os events.

Correlations with the isomeric state of ^{156}Hf must have two intervening β decays, feeding the 9^+ and 8^+ states of ^{156}Ta and ^{156}Hf, respectively. The time delay introduced by these β^+ decays allow significant background contamination through random correlations, from which the signal must be isolated. Correlations with the ground state of ^{156}Hf may come through either of the β^+ decay branches of ^{156}W, provided the β^+ decay of ^{156}Ta feeds the ground state of ^{156}Hf. The half-life of ^{156}W and the branching ratios of the two decay branches of ^{156}W are unknown.

Figure 5.3 shows the Q-values for neutron-deficient osmium isotopes as a function of their mass number. Extrapolating to A=160 suggests an expected Q-value for ^{160}Os in the range 7250 - 7400 keV which corresponds to a predicted half-life between approximately 40 and 90 μs (calculated using Rasmussen's method [21], see section 5.1.4). The correlation time chosen for the recoil-mother decay was therefore chosen to be 100 μs.

Figure 5.4(a) shows all α decays which occurred within 100 μs of a recoil

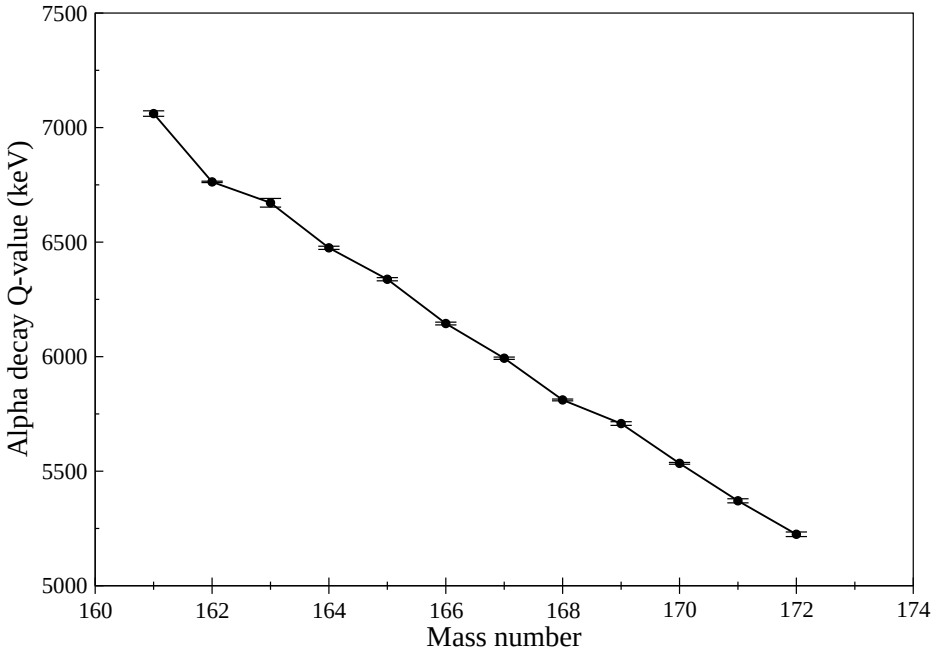

Figure 5.3: *Q-values for neutron deficient osmium isotopes. Values taken from references [2], [13] and [14] and references therein.*

implantation in the same pixel. Figure 5.4(b) is the same as 5.4(a) with the additional requirement that the alpha decay of the recoil is followed within 500ms by one of the decays highlighted in figure 5.2.

The peak occurring at 5910 keV in figure 5.4(b) is the α decay of ^{160}W, which is strongly produced in this reaction and decays to a ^{156}Hf daughter. A similar situation occurs with the small peak at 6530 keV, which is due to ^{160}Re decaying to its ^{156}Ta daughter. The decays of ^{155}Lu and ^{156}Hf visible in this spectrum are due to random correlations. The activity between 6150 and 6400 keV is attributed to the low-energy tail of ^{160}Re and the decays of ^{161}Re (which decays to ^{157}Ta which has an α-decay energy which intrudes on the ^{156}Hf ground state correlation) and ^{159}W (through random correlations).

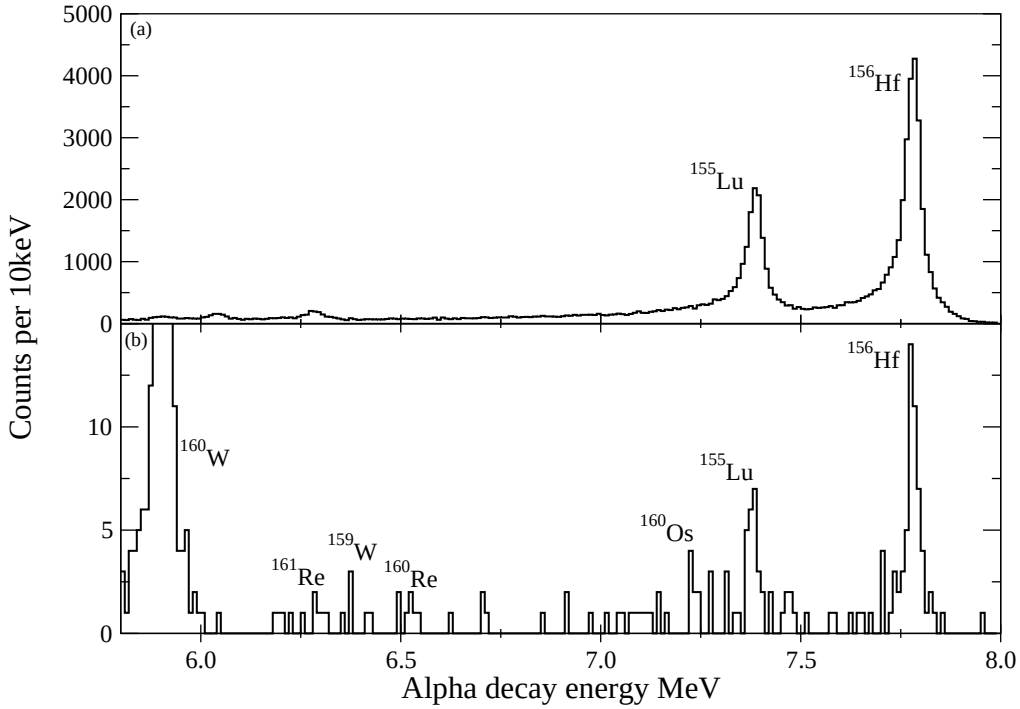

Figure 5.4: *(a) Spectrum of all decays that occur within 100 μs of a recoil implantation in the same pixel. (b) As (a) with the additional requirement that the α decay is followed within 500ms by the ground or isomeric state α decay of ^{156}Hf.*

The activity around 7230 keV is new activity and is tentatively assigned to the ground state decay of ^{160}Os.

5.1.1 LISA veto

^{160}Os is produced in the 4n channel, and so the signal can be emphasised by using LISA to veto any recoils which are temporally correlated with prompt charged particle emission at the target position.

The ^{155}Lu isomer, the most contaminating background channel, is populated in a 2αp channel. The efficiency of LISA was relatively low in this experiment due to a number of detectors not working, but three charged particles

still allows for approximately 75% suppression of this channel (see chapter 4.6).

Figure 5.5 shows the effect of using LISA to veto all charged particle events. The peak assigned to ^{160}Os is emphasised in this spectrum, adding weight to the assignment.

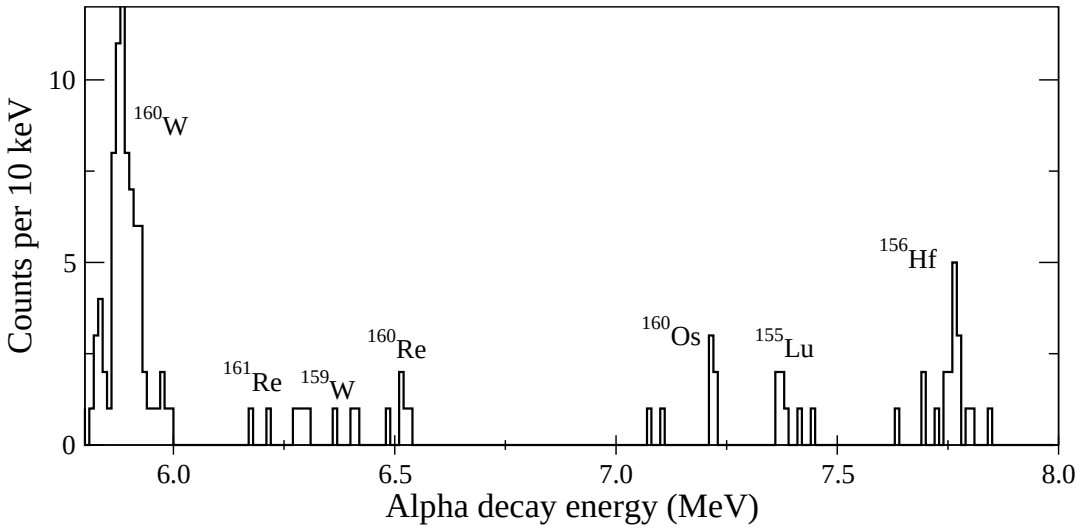

Figure 5.5: *Spectrum of events from figure 5.4(b) which were not coincident with charged particle emission detected at the target position.*

The peak assigned to ^{160}Os in figure 5.5 contains five counts, four from the ^{156}Hf ground state and one from the isomeric state correlations.

There are two counts approximately 130 keV below the main ^{160}Os peak that could also be due to ^{160}Os activity. Activity in that region does not correspond with any known decays that might be produced in this experiment and the lifetimes of the two counts (18 and 28 μs) are consistent with the expected lifetime of the activity in the main peak (see section 5.1.4). However, given the ambiguity of these events they are not included in any further analysis.

5.1.2 Q-value

The Q-values of α decays for nuclei in this region are shown in figure 5.6. A decay energy of 7230 keV for ^{160}Os corresponds to an α Q-value of 7415 keV which is shown with a solid red square. The error can be calculated from other peaks in this data set on the basis that the resolution on this peak is subject to the same limitations as other α decays. Therefore the FWHM of ^{155}Lu events that occur within 100 μs of recoil implantation was used to calculate an error on this measurement of 50 keV.

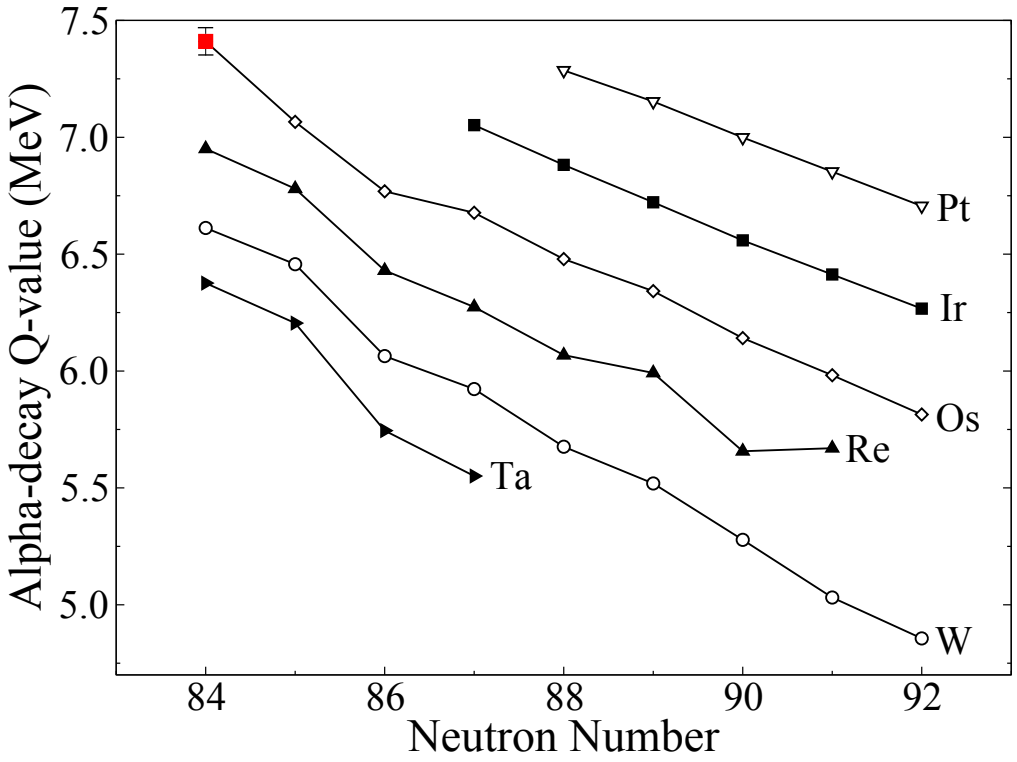

Figure 5.6: *Q-values of α decays of $\pi h_{11/2}$ states in odd-Z nuclei and the ground states of even-Z nuclei. The value for ^{160}Os, taken from the present work, is highlighted with a solid red square. The other values are from references [2, 7, 13–15, 18, 36–51].*

The Q-value is approximately 100 keV higher than would be expected from

systematics since it does not show the same levelling off with decreasing neutron number that is observed in the rhenium, tungsten and tantalum isotopes. This discrepancy is a reason to be cautious about the assignment, or it may indicate that ^{160}Os is less tightly bound than expected. A possible physical explanation is discussed in section 7.

5.1.3 Background analysis

The ^{160}Os signal is situated in the low-energy tail of ^{155}Lu which, along with the ^{156}Hf peak, appears in these spectra due to false correlations. False correlations occur when a series of unrelated events are mis-assigned as a recoil-mother-daughter correlation. There are two main mechanisms which may produce a false correlation that fits the search criteria. Firstly, a 100 μs recoil-α correlation interrupts a separate decay chain that leads to the decay of ^{156}Hf or ^{156m}Hf. Secondly, if there are two consecutive decay chains, where the recoil implantation of the latter is unseen (most likely due to detector dead time) and where the latter leads to the decay of ^{156m,156}Hf. Figure 5.7 illustrates these mechanisms.

The false correlations illustrated in figure 5.7 can be reproduced by searching for the daughter correlation in a different pixel to the recoil implantation. Given that the range of the α particle is much less than the width of a pixel the probability of an alpha decay being detected in a pixel from which it did not originate is negligible. This means that no real correlations will be found using these search conditions while the false correlations are produced with the same probability.

Figure 5.8 shows the same spectrum as shown in figure 5.5 overlayed in blue with the spectrum of events obtained using same conditions, except that the daughter must be found in a different pixel to the one in which the 100μs

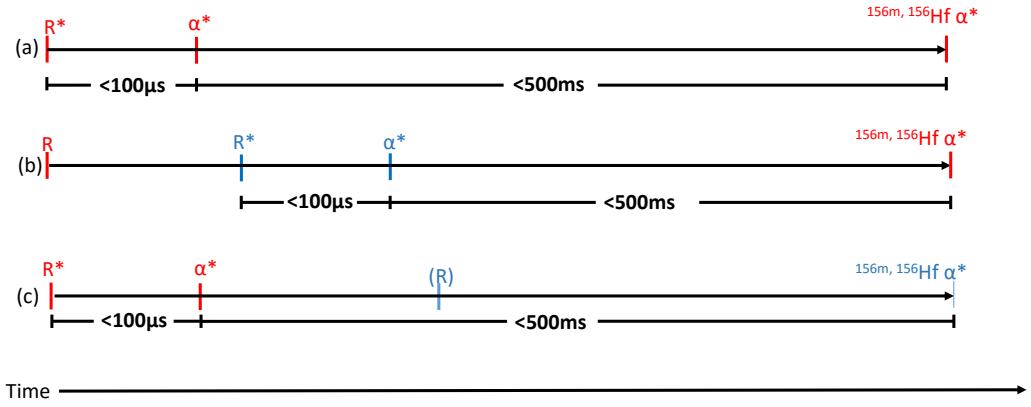

Figure 5.7: *An illustration of the conditions which a series of hits must pass in order to be designated as a recoil-mother-daughter correlation. Events represented using the same colour are physically related. Asterisks denote events which are assigned as part of a correlation. A bracket denotes an event which is missed by the strip detector. Thus (a) represents the ideal case, in which the correlated events form a true recoil-mother-daughter correlation while (b) and (c) show ways in which a false correlation may occur.*

recoil-α correlation was found. The background spectrum was summed over all possible pixels and normalised to the ^{156}Hf peak. It accurately reproduces the other significant false correlation, ^{155}Lu, while the real activity occurring due to the ^{160}W and ^{160}W α decays (see figure 5.2) disappears completely. Similarly, the peak at 7230 keV disappears suggesting that it is due to real activity and adding further weight to the ^{160}Os assignment.

The background spectrum contains 0.4 counts in the energy region associated with the ^{160}Os peak in figure 5.5. The possibility of 5 counts being observed in this region due to a statistical fluctuation of the background can be excluded with 99% confidence [52].

However, analysis of the α - α time spectrum (i.e. the time between the ^{160}Os candidate α decay and the α decay of the daughter correlation) casts some doubt on the tentative assignment. From figure 5.2 the α - α time would be expected to be of the order of 100s of milliseconds.

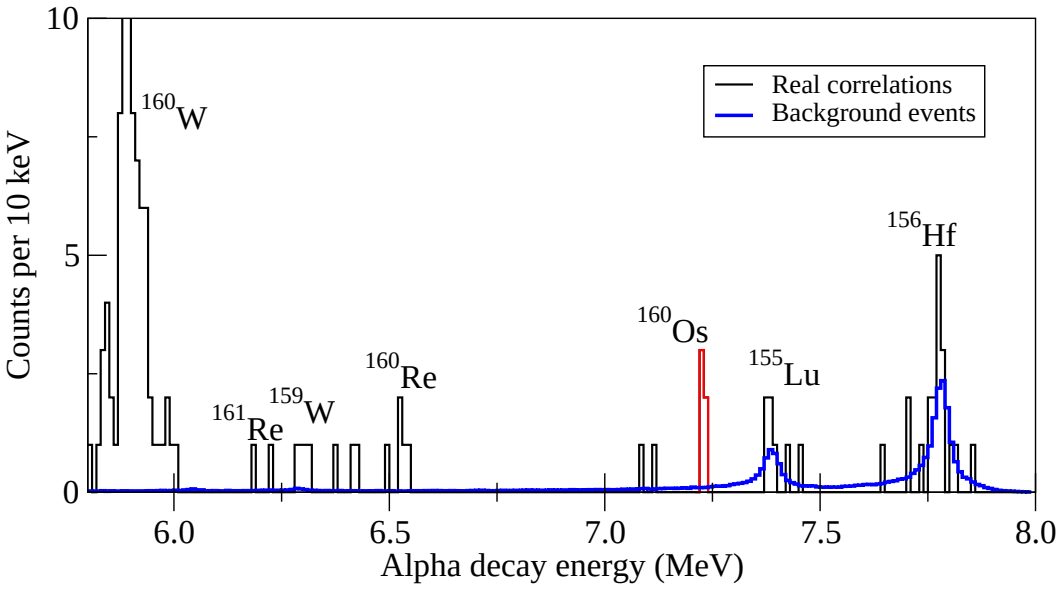

Figure 5.8: *The same spectrum that is shown in figure 5.5 overlayed with a background spectrum (blue). The background spectrum was obtained by searching for the daughter correlation in a different pixel to the recoil implantation, summing over all pixels and normalising to the* ^{156}*Hf peak. See text for discussion.*

The α - α time for the single count correlated with the ^{156}Hf isomer is consistent with this at 495ms and remains a strong candidate.

However, the α - α times for the four counts correlated with the ^{156}Hf ground state are 0.7, 26, 30 and 78 ms, with a mean half-life of 23ms. The mechanism for generating background shown in figure 5.8(b) requires a recoil-α correlation with an α decay energy that could be ^{160}Os that interrupts a separate decay chain that leads to ^{156}Hf. Given that the half-life of ^{156}Hf is 23(1) ms the α - α times for this correlation are more consistent with background than the proposed assignment. There is a further test that can be performed: if the counts are being generated through this background mechanism then there should be an additional recoil implantation (the ^{156}Hf recoil) occurring prior to the recorded recoil-mother-daughter correlation, and should occur within a time consistent with the life time of ^{156}Hf (23 ms). Therefore

the possibility of this background mechanism but can be tested by measuring the time between the observed recoil-mother-daughter correlation and the last recoil to be implanted in that pixel. If the distribution is comparable to the half life of ^{156}Hf then it supports the background hypothesis. If the distribution is comparable to the implantation rate of 0.5 Hz then the background hypothesis is doubtful. The observed time periods between the previous recoil implantation in the same pixel for the four ^{156}Hf ground state correlations were 1, 16, 110 and 668 ms. 1 and 16 ms are consistent with background, 110 ms is at the edge of distribution and 668 ms is inconsistent with background. The previous recoil time for the count correlated with the ^{156}Hf isomer was 1700ms, and so this count remains a strong candidate.

5.1.4 Half-Life

In order to measure the half-life the recoil-mother correlation time was extended to 300 μs, no additional counts were found in the ^{160}Os energy region using this extended correlation time. Using the five counts seen in figure 5.5 the half-life was measured using the method of maximum likelihood outlined in reference [53] to be 35^{+19}_{-15} μs. Figure 5.9 shows the predicted half lives of a ΔL=0 α decay as a function of Q-value, calculated using Rasmussen's method [21]. The measured value is consistent with the predicted value for an α decay of this Q-value.

^{155}Lu has a half-life of 2710 μs [14], and when the half-life is measured using a maximum likelihood method from a sample of correlations confined to less than 300 μs without correcting for the measurement interval the expected value of the measurement would be 103 μs. The value measured for the events in ^{155}Lu energy region is consistent with this value, at 123^{+29}_{-20} μs. The fact that the half-life measured for the events attributed to ^{160}Os is inconsistent with

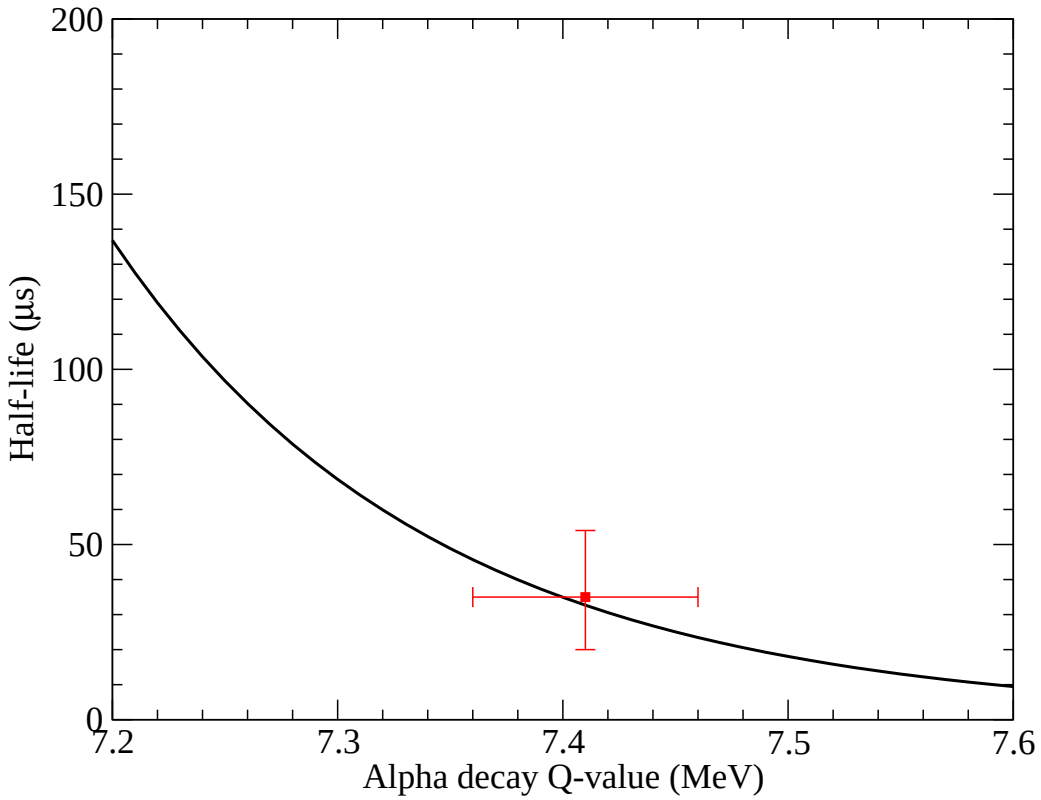

Figure 5.9: *Predicted half-lives of α decays as a function of Q-value for ΔL=0, using Rasmussen's method [21] with the measured values of the ^{160}Os Q-value and half-life shown in red.*

expected value for ^{155}Lu decays adds further weight to the assignment.

Plotting the decay times of an exponential decay along a logarithmic x-axis produces a broad peak of universal shape with a maximum at the mean lifetime [54]. Figure 5.10 shows such a plot for the ^{155}Lu, ^{156}Hf and ^{160}Os energy regions of figure 5.5 with the maximum recoil-mother time difference extended to 10ms. The x-axis is $\log(dT/10$ ns) where dT is in units of 10 ns (the precision of the TDR), thus a value of 6 on the x axis corresponds to a time difference of 10 ms. The red overlay represents the shape of the curve that would be expected assuming the number of events in the measured spectrum. Note that because the overlay is not fitted to the data (but rather is a separate

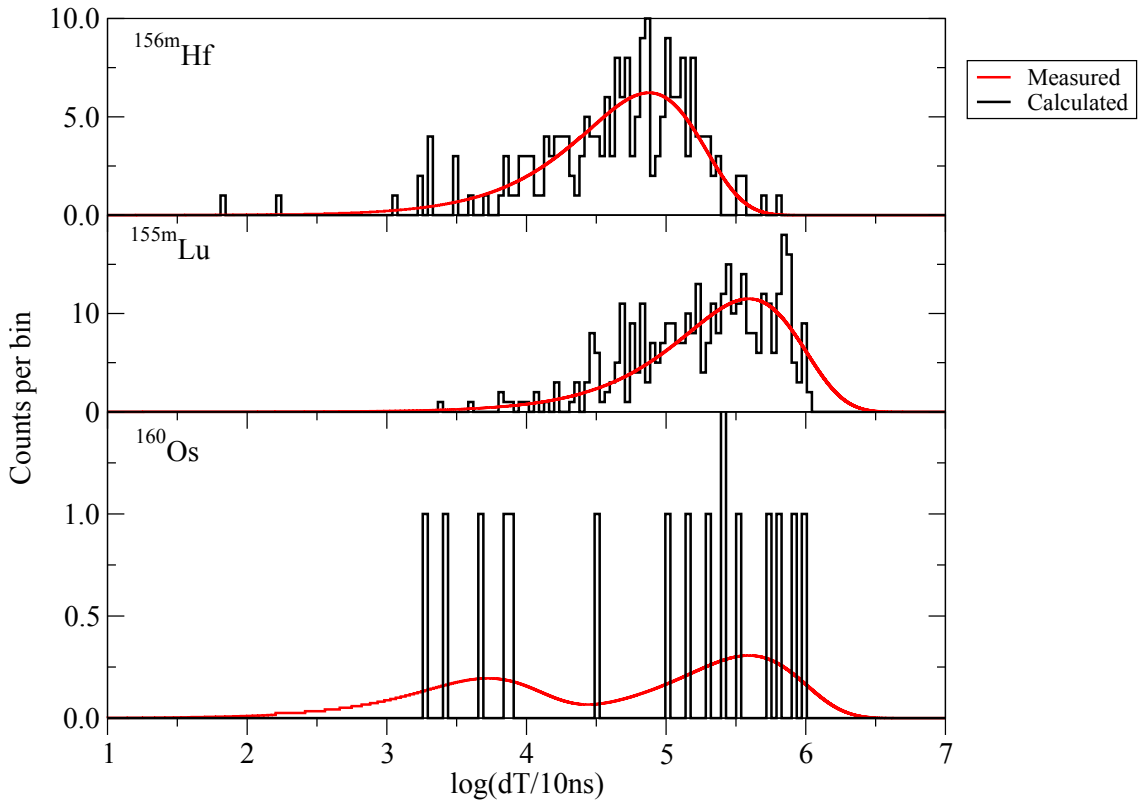

Figure 5.10: *log(dt) plots for the recoil-mother decay times of counts taken from the ^{160}Os ^{155}Lu and ^{156}Hf energy regions of figure 5.5 with the maximum recoil-mother time extended to 10 ms. Time difference is in units of 10 ns. The red overlay is the shape that would be expected for decays of the relevant nucleus, assuming the number of counts seen in the measured spectrum. The calculation for the bottom plot assumes 6 counts of ^{160}Os and 10 counts of ^{155}Lu based on the background spectrum. See text for discussion.*

function) it is not skewed by plotting it for values greater than 10 ms. For the ^{155}Lu and ^{156}Hf graphs the overlay is the function

$$n\lambda t \times e^{-\lambda t} \tag{5.1}$$

where n is the number of counts in the measured spectrum, t is the decay time and λ is the decay constant of that nucleus. The red overlay in the ^{160}Os spectrum assumes a mixture of ^{160}Os and ^{155}Lu background and is given by

$$n_1\lambda_1 t \times e^{-\lambda_1 t} + n_2\lambda t \times e^{-\lambda_2 t} \tag{5.2}$$

where λ_1 and λ_2 are the decay constants and n_1 and n_2 are the number of counts of ^{160}Os and ^{155}Lu respectively. The background spectrum generated in section 5.1.3 predicts 10 counts of ^{155}Lu in the ^{160}Os energy region. There are 16 counts in figure 5.10 hence n_1 and n_2 are assigned the values of 6 and 10 respectively. The data in the lower plot corresponds better to the curve that has been plotted (which represents a mixture of ^{160}Os and ^{155}Lu) than it would to a curve consisting only of ^{155}Lu.

5.1.5 Production cross Section

The detection efficiency is taken to be approximately 20% (based on a 40% transmission efficiency through RITU and 50% efficiency for detecting the recoil-mother-daughter correlation in the DSSDs). The correlation time used is approximately equal to three half lives of ^{160}Os from the measurement made in this work. The observation of five counts of ^{160}Os therefore leads to an estimate of 30 ^{160}Os nuclei produced in this experiment in total. This gives a production cross section at this beam energy of about 0.1 nb, with an estimated uncertainty of factor of two. This is somewhat lower than the 4 nb measured for the production of ^{166}Pt through a 4n channel measured in reference [18] and may reflect a beam energy that is higher than the optimum value.

5.1.6 Contribution from ^{156}Ta proton correlation

The ^{160}Os signal was found using ^{156}Hf and ^{156m}Hf correlations as highlighted in figure 5.2. Correlations with the proton emission from ^{156}Ta were also sought.

Figure 5.11 shows the spectra associated with each separate correlation,

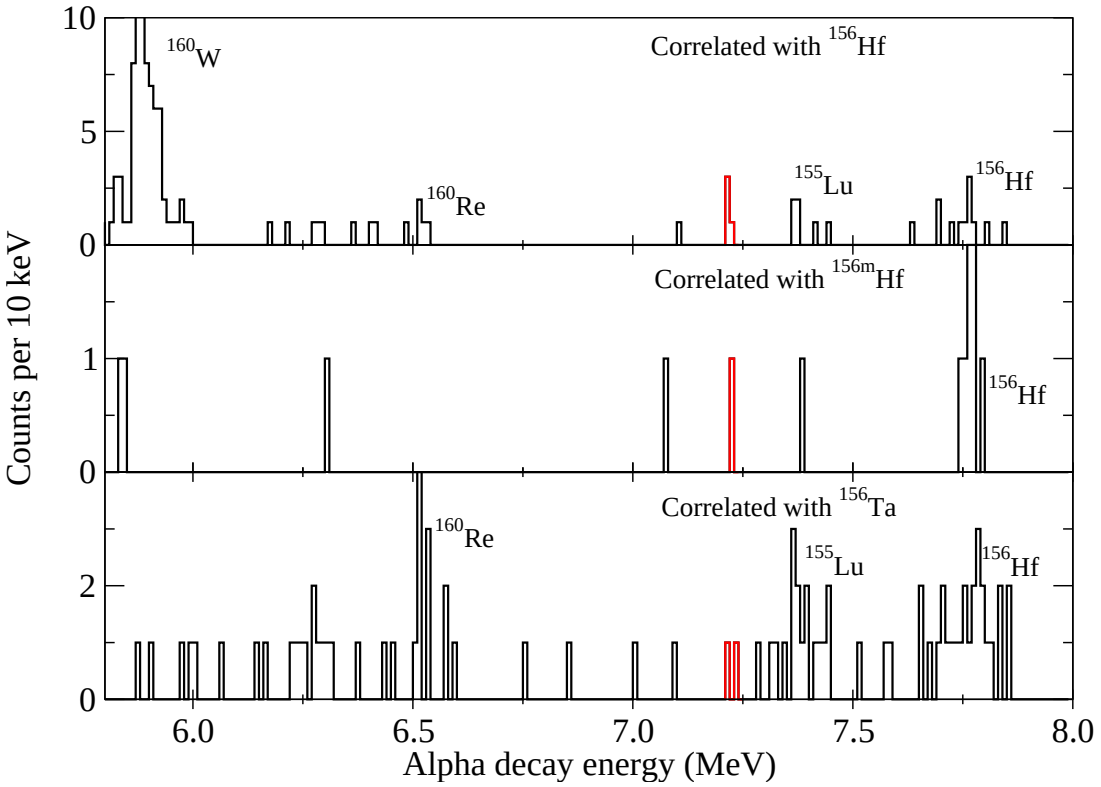

Figure 5.11: *Events occurring within 100μs of a recoil implantation followed within 500ms by the described correlation. Events are LISA vetoed as in figure 5.5 and the events that might be attributed to ^{160}Os are highlighted in red.*

such that the sum of the ^{156}Hf and ^{156m}Hf spectra from figure 5.11 gives the spectrum shown in figure 5.5. While the ^{156}Ta correlation contains two counts within the energy region attributed to ^{160}Os it can be seen that this correlation introduces much more background than the other spectra. This is because the energy of the ^{156}Ta proton emission sits in the spectrum of escaped α decays and it is not possible to distinguish proton decays of ^{156}Ta from escaped α decays that deposit the same energy. The problem is then twofold:

1. False correlations due to unrelated decay chains that match the search criteria (see figure 5.7) become more probable because the false correlation does not have to lead to a ^{156}Ta proton emission, but merely something that

looks like a ^{156}Ta proton emission.

2. False correlations that occur when the search critera correctly match a recoil-mother-daughter decay chain but the daughter is mis-assigned as a ^{156}Ta decay.

These mechanisms do not significantly affect the ^{156}Hf and ^{156m}Hf correlations because there are no candidates such that the daughter decay in a recoil-mother-daughter chain is higher in energy than the ^{156}Hf decay for which it might be mistaken. It should also be noted that the previously described method for predicting background by searching in a separate pixel cannot account for the background introduced through the 2nd point, since this relies on the recoil, mother and daughter decay all being physically related to one another, even if the daughter decay is mis-assigned. For this reason there is no overlay of the predicted background in figure 5.12.

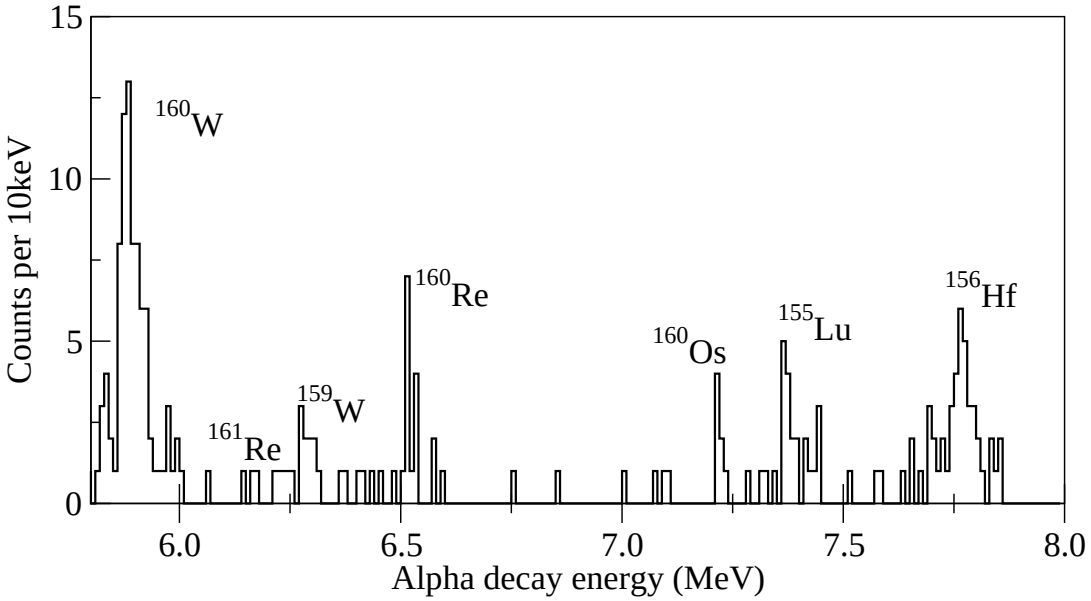

Figure 5.12: *Events occurring within 100μs of a recoil implantation followed within 500ms by ^{156}Hf or ^{156m}Hf α decays or ^{156}Ta proton decay.*

Figure 5.12 shows all 3 spectra from figure 5.11 summed together, i.e a

LISA-vetoed 100 μs recoil α correlation followed within 500 ms by either ^{156}Hf, ^{156m}Hf or ^{156}Ta. When compared to figure 5.5 the peak assigned to ^{160}Os contains two extra counts but the signal to background ratio is poorer due to the extra background introduced through the ^{156}Ta correlation, therefore the analysis in this chapter uses only the five counts from the ^{156}Hf and ^{156m}Hf correlations.

5.1.7 Search for the Expected 8^+ Isomer

The α decays of the isomeric states of the N=84 isotones ^{158}W and ^{156}Hf are 1850 and 1910 keV higher than their respective ground state decays [14]. An α decay of the isomeric state of ^{160}Os would be expected to have a decay energy of about 9.2 MeV. No activity was found in this region even with the recoil-mother correlation time extended to 10 ms to allow for the possibility of the isomer being longer lived than the ground state (see figure 5.13).

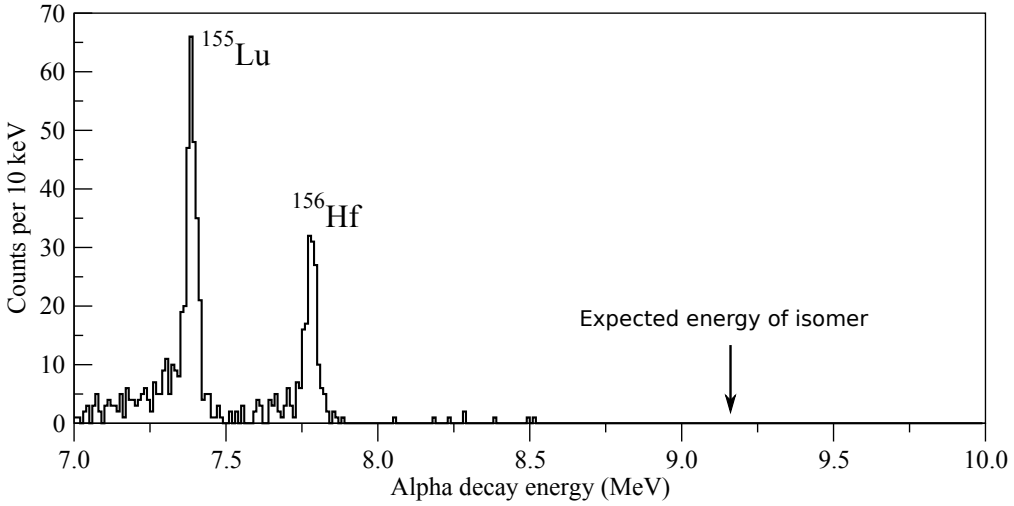

Figure 5.13: *The high energy region of figure 5.5 with the recoil-mother correlation time extended from 100μs to 10ms. The isomer decay energy would be expected to be around 9.2 MeV.*

If the 8^+ state of ^{160}Os is a two-proton emitter then it would populate the ground state of ^{158}W, which would emit a 6445 keV α with a half life of 1.5 ms [13]. No evidence of this scenario has been found in these data.

Chapter 6

Spectroscopy of ^{159}Re and ^{155}Ta

^{159}Re is the heaviest N=84 isotone for which spectroscopic information is known. Previous works [6, 7] have identified α and proton decays which have been classified as emanating from the $h_{11/2}$ orbital based on comparison between predicted and measured values of the half life (see chapter 7). In addition to decays emanating from an isomeric $h_{11/2}$ state it is expected to have an αd $25/2^-$ isomer and a proton-emitting $s_{1/2}$ ground state with a life time of approximately 10 ns (see chapter 1) neither of which have yet been observed. In this chapter improved measurements of the α decays from the $h_{11/2}$ state, evidence of a possible α decay emanating from a $25/2^-$ state, and a spectrum of γ decays above the $h_{11/2}$ state are presented. Improved measurements of the proton emission of ^{155}Ta the α decay daughter of ^{159}Re are also presented. The implications of these findings are discussed in chapter 7.

^{159}Re undergoes proton emission from the isomeric $h_{11/2}$ state with an energy of 1805(20) keV [6]. The same state is reported to undergo α decay [7] with a branching ratio of 7.5(3.5)% and an energy of 6776(26) keV. Both references made consistent measurements of the half-life of the state of 21(4) and 16(9) μs. The daughter of ^{159}Re is ^{155}Ta which undergoes proton emission with

an energy of 1444(15) keV and a half-life of $2.9^{+1.5}_{-1.1}$ ms [7]. This information is summarised in figure 6.1.

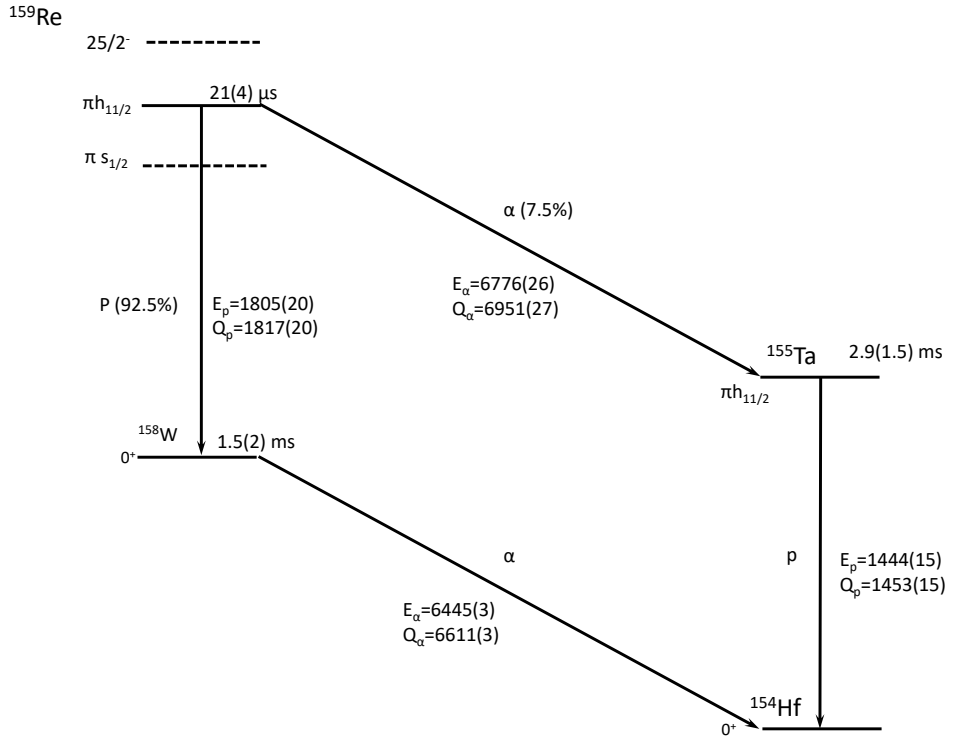

Figure 6.1: *Known decays emanating from the $\pi h_{11/2}$ orbital of ^{159}Re and subsequent nuclei, values taken from references [13], [7] and [6]. Dashed lines represent states that are predicted to exist but have not yet been observed.*

The work outlined in this chapter was done in parallel with Dr. Edward Parr. The section on the γ rays above the $h_{11/2}$ state (section 6.1.2) and the evidence for a possible $25/2^-$ isomer (section 6.1.3) were done primarily by the author. In section 6.1.1 the data were sorted and the figures produced by the author, but for the sake of consistency the measurements of half-lives, energies and branching ratios presented here were done by Dr. Parr.

6.1 Results

The results presented in this work were obtained from the same experimental work as was described in chapter 5. Charged particle events were detected in the DSSDs and γ rays were detected in Jurogam. The signals of interest were isolated from the large background using the MWPC, PIN diodes, TAC measurements, and DSSD signals as outlined in chapter 4.

6.1.1 Improved spectroscopic measurements of known α and proton decays

Previous works on the decay modes assigned to the $h_{11/2}$ state in ^{159}Re found approximately 50 correlated ^{159}Re proton events [6] and five ^{159}Re α decay events [7]. In this work a different beam energy, longer experiment, and reduced dead time has allowed for roughly an order of magnitude improvement on these statistics.

Table 6.1: Summary of decay data from this work compared to literature values for ^{159}Re and ^{155}Ta.

	Literature	This work
^{159}Re		
Half life (μs)	21(4)	21(1)
Alpha decay energy (keV)	6776 (26)	6818(6)
Proton decay energy (keV)	1805(20)	1802(2)
Branching ratio (α/proton)	7.5/92.5 %	5.0(8)/95(4)%
^{155}Ta		
Half life (ms)	2.9(1.5)	3.3(6)
Proton decay energy (keV)	1444(5)	1429(5)

Recoil-mother-daughter correlations were used to analyse these decay modes, with time gates selected to emphasise the ^{159}Re $h_{11/2}$ state, and the PIN diodes

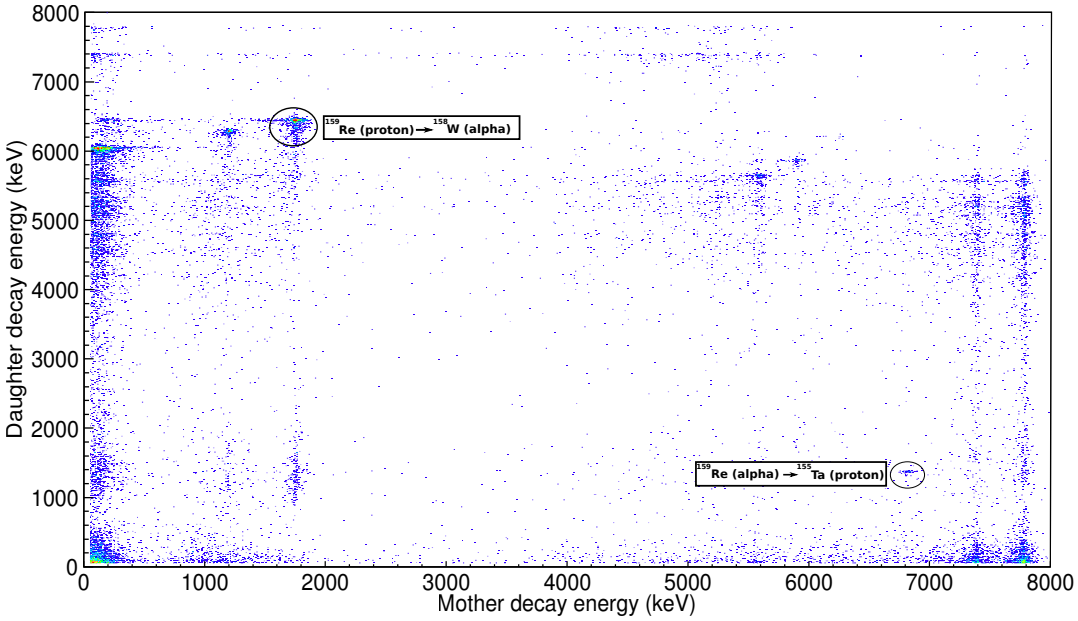

Figure 6.2: *Daughter energy vs mother energy with time gates selected to emphasise the* ^{159}*Re* $h_{11/2}$ *decays.*

used to suppress background by vetoing events that fail to deposit their full energy in the DSSD. Figure 6.2 shows the daughter energy plotted against the mother energy of recoil-mother-daughter correlations and highlights the events corresponding to the proton- and α-decay modes of ^{159}Re.

Figure 6.3 shows the ^{159}Re α decay (a) and proton decay events (c) and the ^{155}Ta proton decay events (b), found using the appropriate time gates and mother or daughter energy gate.

The order of magnitude improvement in statistics in this data set was used to make improved measurements of the properties of these decay modes, using the maximum likelihood method [54] for half-lives. ^{159}Re was measured to have an α decay energy of 6818(6) keV (branching ratio 5.0(8)%), a proton decay energy of 1802(5) keV (branching ratio of 95(4) %), and a half-life of 21(1) μs. The proton decay of ^{155}Ta was measured to have an energy of 1429(5) keV

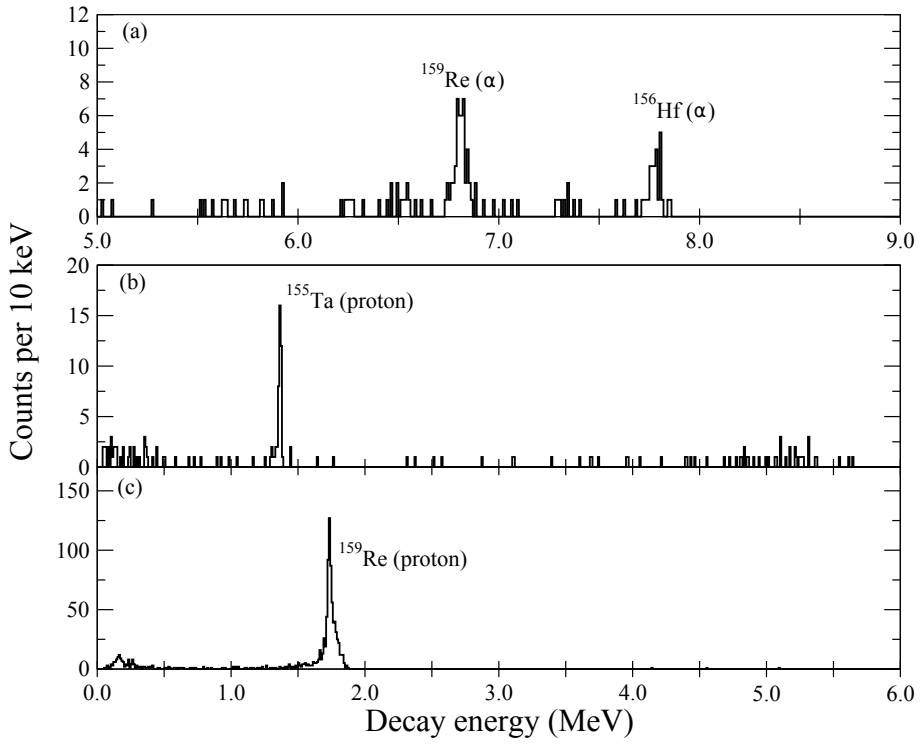

Figure 6.3: *(a) Events occurring within 100 μs of a recoil implantation followed within 12 ms by the proton emission of ^{155}Ta. (b) The corresponding daughter correlation to (a), i.e. events that occur within 12 ms of a ^{159}Rerecoil-α decay correlation. (c) Events within 100 μs of a recoil implantation that are followed within 10ms by the α decay of ^{158}W*

and a half-life of 3.3(6) ms. These values are summarised in table 6.1 and are broadly consistent with the measurements made in references [6] and [7]. It's true that there is approximately a two σ discrepancy between the values of the α decay energy of ^{159}Re, but there is reason to be cautious about the literature value since it is based on only five counts, and the short life time means that base the base line correction is significant and and may introduce additional uncertainty.

No evidence of the proton decay of ^{155}Ta reported in reference [8] was found.

6.1.2 γ rays above the $h_{11/2}$ state

The RDT method (see chapter 4) was used to find γ rays coincident with the α and proton decays assigned to the $h_{11/2}$ state of ^{159}Re. Using only the decay of ^{159}Re is insufficient for proper identification of this nucleus due a low production cross section compared to other products of this reaction, and recoil-mother-daughter correlations were necessary to identify ^{159}Re events unambiguously. Figure 6.4 is the results of all events using both proton and α decay lines. To produce this spectrum the PIN diode add back techniques outlined in chapter 4 were used for all combinations of mother and daughter escapes, increasing statistics by almost a factor of two.

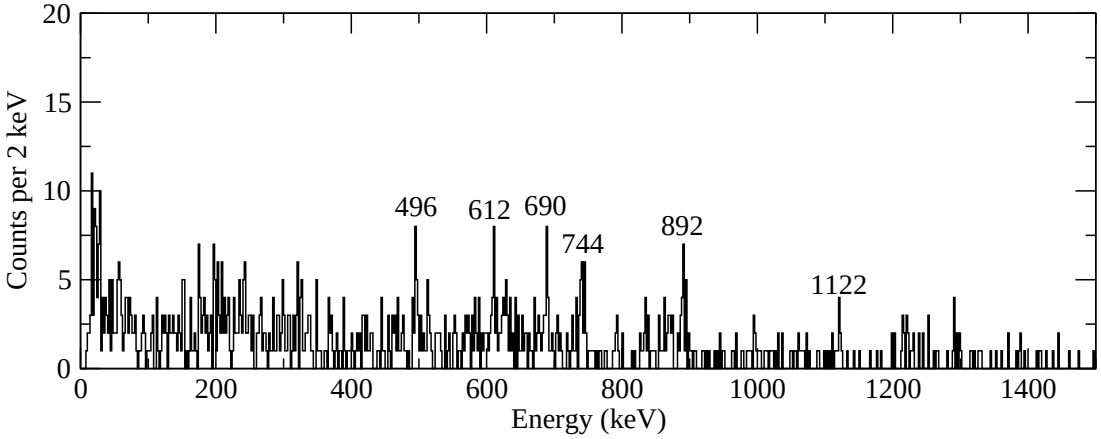

Figure 6.4: *γ rays assosciated with with $h_{11/2}$ state of ^{159}Re. Peaks are labelled with energies in keV.*

A discussion of the ordering of the transitions seen in figure 6.4 and comparison to the lighter N=84 isotones can be found in chapter 7.

6.1.3 Search for the Expected $25/2^-$ Isomer

An α decaying isomeric state in ^{159}Re may populate the 11/2 ground state of ^{155}Ta which would then undergo the known proton emission (see figure 6.1).

Figure 6.5 shows all decays that occurred within 4 ms of recoil implantation and are followed within 12 ms by the proton decay of ^{155}Ta (all events are PIN vetoed)

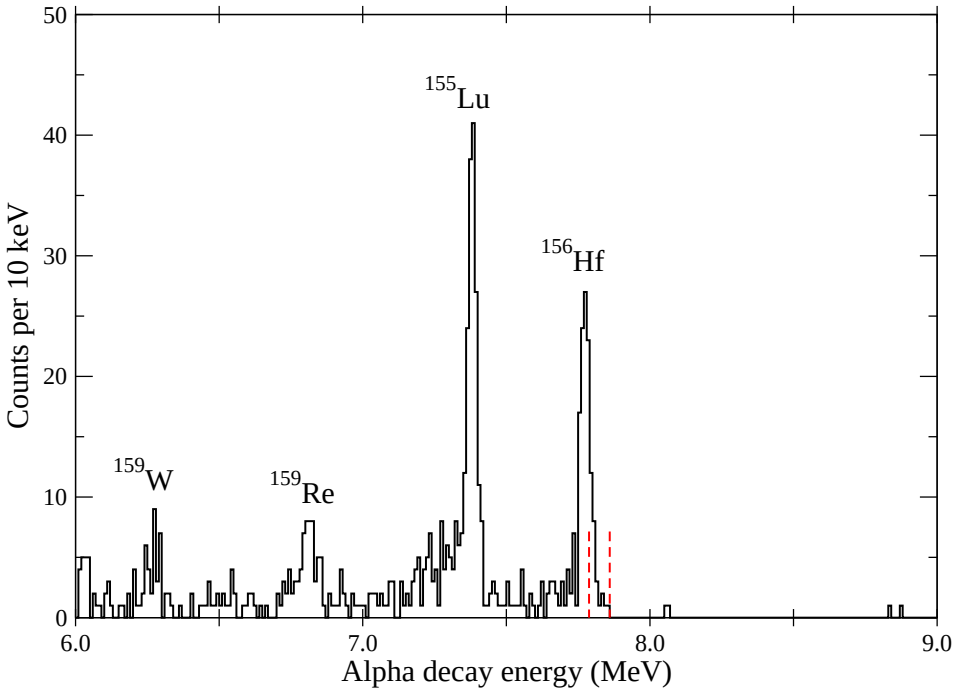

Figure 6.5: *All decays that occur within 4 ms of a recoil implantation and are followed within 12 ms by the proton emission of ^{155}Ta. The dashed red lines highlight the energy gate used in the bottom spectrum of figure 6.6.*

In this spectrum there are no obvious candidates for an α-decaying ^{159}Re isomer.

However, further analysis shows evidence that the isomer may be hidden behind the ^{156m}Hf peak. The top spectrum of figure 6.6 shows the ^{155}Ta peak that emerges when gating on the ^{159}Re $h_{11/2}$ α decay. The black line of the bottom spectrum shows the result of gating on the high-energy portion of the ^{156}Hf peak, from 7800 to 7860 keV, with time gates of 4 ms and 12 ms for the mother and daughter correlations respectively. The energy gate used is

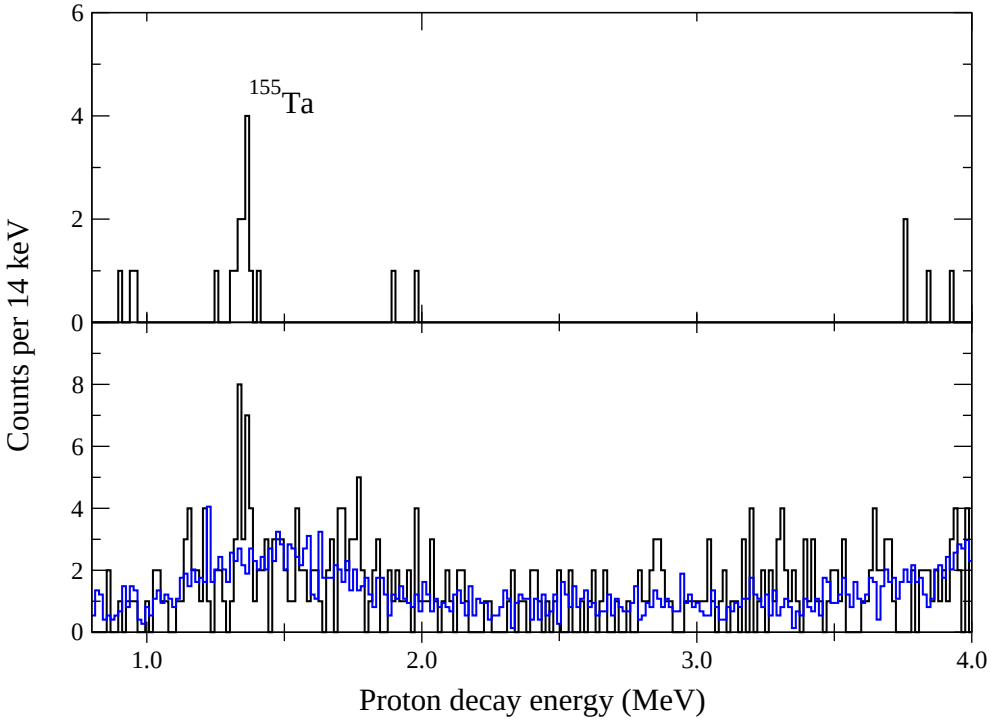

Figure 6.6: *Top: decays that occur within 12 ms of a recoil-α chain that matches the time and energy conditions of a* ^{159}*Re* $h_{11/2}$ *α decay. Bottom: decays that occur within 12 ms of an α decay with an energy that falls within the energy gate highlighted in figure 6.5 and a recoil-mother time gate of 4 ms. The blue overlay is expected background achieved by gating on the lower energy region of the* ^{156}*Hf peak.*

highlighted with dashed red lines in figure 6.5. The blue overlay is the expected background of this spectrum, found using the same search conditions except the correlation energy gate was set to a lower energy region of the ^{156}Hf peak, and normalised using the spectrum of beta decays (out of the range of this figure).

There is evidence of a peak emerging with an energy that matches the ^{155}Ta proton emission that is not reproduced in the background spectrum. While the fact that it emerges with the correct energy is promising the number of counts is not far above background: 27 counts compared to 16 in the background

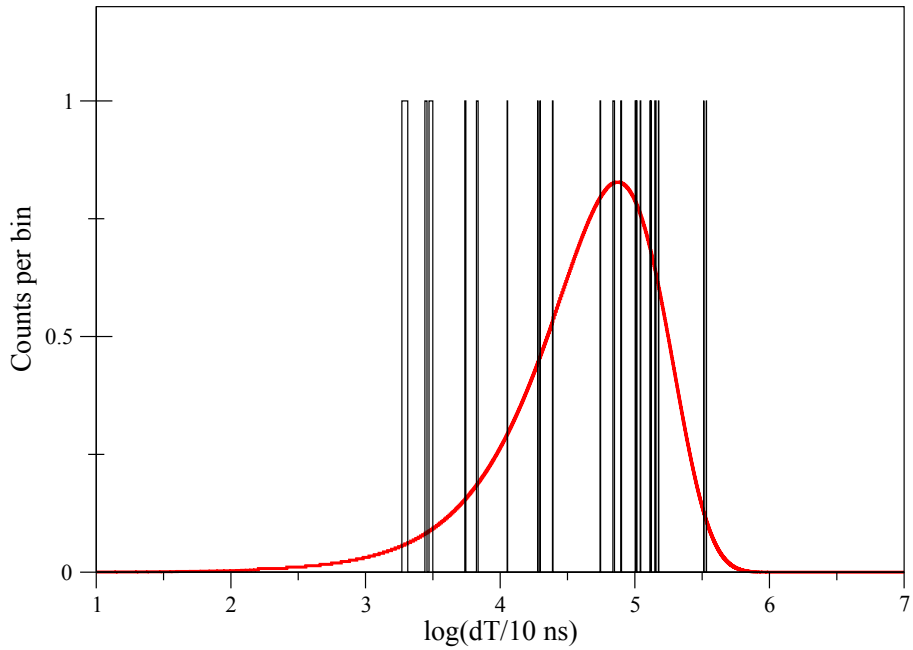

Figure 6.7: *Decay times for candidates for a ^{159m}Re α decaying isomer plotted on a logarithmic x-axis. dt is in units of 10 ns. The red line denotes the expected distribution of decay times for the background. See text for discussion.*

spectrum, which is within the range of statistical fluctuations. The assignment is therefore tentative.

Figure 6.7 shows the decay times (plotted on a logarithmic axis) for the isomer candidates shown in the highlighted region of figure 6.5. The red line denotes the expected distribution for ^{156m}Hf events (i.e. the expected background), from which the observed decay times do not markedly deviate. However a ^{159}Re isomer with the same decay energy would likely have a half-life that is comparable to the half-life of the corresponding isomer in the Z=72 isotone and so this spectrum is not detrimental to the tentative assignment.

Chapter 7

Discussion

7.1 ^{160}Os Assignment

The results laid out in chapter 5 provide evidence for the discovery of the ground state α decay of ^{160}Os . The signal appears with an energy and half-life that are consistent with the expected values in a region where there is not expected to be any other activity, and where the background due to false correlations is below the observed signal. The signal is emphasised by the use of a LISA veto which is consistent with a neutron-only evaporation channel. Doubt is cast on the assignment, however, by the short α - α times which are more consistent with the expected source of background. One explanation for the short α - α times could be a biased distribution. The longer the time period between the mother and daughter decays the more likely that the chain will be interrupted and evidence of the correlation lost. However it is questionable whether this effect could account for the magnitude of the observed discrepancy. An alternative explanation is that the low value is due to statistical fluctuation, given the small number of events.

Other reasons to be cautious about the assignment include the fact that the

expected isomer has not been observed and the Q-value is approximately 100 keV higher than would be expected from systematics since it does not show the same levelling off with decreasing neutron number that is observed in the rhenium, tungsten and tantalum isotopes (see figure 5.6). Possible physics explanations for these observation are discussed in this chapter within the context of the assumption that the observed signal is indeed the ground state decay of ^{160}Os .

The high Q-value suggests that ^{160}Os is less tightly bound than expected. Reference [55] discusses the manner in which the mixing of nucleon orbitals modifies the energy of excited states, in some cases to a sufficient degree that shape coexistance emerges due to the degeneracy of energy levels that would otherwise be well separated. Specifically, when particle-hole excitations occur across shell gaps the cost of energy to redistribute nucleons from a spherical to a deformed configuration is set against the gain in energy from residual interactions between nucleons (correlation energy). If the correlation energy of an excited configuration with a given number of particle-hole pairs (np-nh) is large enough then an intruder state may be energetically favourable. For example, calculations show that in ^{40}Ca the 4p-4h and even 8p-8h 0^+ states are lowered by the interaction energy between nucleons in the upper part of the *sd* shell and the full fp shell to the degree that the excitation energy is not far above that of the spherical configuration. It is possible that the increased Q-value of ^{160}Os is driven by a similar mechanism involving the nucleon-nucleon interaction energy. In ^{156}Hf and ^{158}W there is a decrease in the energy gap between the lowest lying neutron orbitals above the N=82 shell closure, $\nu h_{9/2}$ and $\nu f_{7/2}$ [16]. This results in greater mixing between these orbitals and a correspondingly higher correlation energy leading to a more tightly bound ground state and lower Q-value. The observation of a less

tightly bound ground state in ^{160}Os would imply that the trend of decreasing energy gap between the $\nu h_{9/2}$ and $\nu h_{9/2}$ orbitals is reversed in ^{160}Os, with a wider energy gap resulting in less mixing and a smaller correlation energy.

7.1.1 High spin isomer in the N=84 isotones

With Z=76 and N=84 ^{160}Os has 12 protons and two neutrons above a ^{146}Gd core. The valence space for protons consists of the $h_{11/2}$, $s_{1/2}$ and $d_{3/2}$ orbitals while the neutrons occupy the $f_{7/2}$ and $h_{9/2}$ orbitals. The origin of the isomer in the lighter even-Z N=84 isotones is the excitation level of the 8^+ state falling below the 6^+ state due to the interaction between the $h_{9/2}$ neutron and the $h_{11/2}$ protons.

The lack of observation of the isomer in ^{160}Os may be due to a very short lifetime. In this experimental set up the DSSDs had a minimum of 7μs period of dead time after recoil implantation. An isomer with a lifetime which is smaller than this dead time would be very difficult to observe with such low statistics. Equally, the isomer may be much longer lived than expected which would correspond to a lower Q-value. In this case it is possible that the signal would be lost behind the ^{155}Lu or ^{156}Hf peaks, or that the background introduced by the longer correlation time would render the signal unobservable.

It is also possible that the isomer does not exist. If in ^{160}Os either the 6^+ state has decreased or the 8^+ state has increased in excitation energy relative to the previous even-Z isotone (see figure 1.4) then the 8^+ state would no longer be isomeric. An increase in the 8^+ state may be due to a reduction in the strength of the interaction between the $h_{9/2}$ neutron and the $h_{11/2}$ protons caused by the increased occupation of the $\pi h_{11/2}$ orbital and the lack of available holes into which protons may scatter. A decrease in the excitation energy of the 6^+ state may be due to mixing of the $h_{9/2}$ and $f_{7/2}$ neutron orbitals in the 8^+

state.

In Chapter 6 the evidence for the corresponding isomer in ^{159}Re is discussed. While there appears to be some evidence for such an isomer the assignment is tentative and it may be that the lack of a strong candidate for the ^{159}Re isomer is caused by the same phenomenon that results in a lack of observation of an ^{160}Os isomer. This would suggest that adding any further protons to ^{158}W has the effect of either making the isomer unobservable in this work (so short lived that it is lost in dead time, or so long lived that it is lost in background or the correspondingly low Q-value causes it to be hidden behind other α decays) or resulting in a change of structure that renders the state non-isomeric.

7.1.2 Decays emanating from a ^{159}Re $h_{11/2}$ orbital

The half-life measurements of the proton decay and α decay of ^{159}Re were consistent with one another and the total Q-value of each decay chain, from the ^{159}Re decay to the ^{154}Hf ground state, were consistent with one another (8421(6) keV for the ^{159}Re proton chain and 8428(8) keV for the ^{159}Re α chain). These observations confirm the claim made in reference [7] that both decays emanate from the same state. The assignment to the $\pi h_{11/2}$ orbital was made in reference [6] based on the compatibility between the observed half-life of the proton emission and the half life predicted by WKB calculations for a proton decay of the observed energy from the $h_{11/2}$ orbital, and incompatibility with other possible orbitals.

The γ rays above the $h_{11/2}$ state as identified in chapter 6 are shown in the lower part of figure 7.1 (reproduced from figure 6.4). The statistics are too low in this work for γ-γ coincidences to be used to identify the order in which these transitions occur above the $h_{11/2}$ state, but comparisons may be drawn with the lighter odd-Z isotone ^{157}Ta. A level scheme for ^{157}Ta was identified

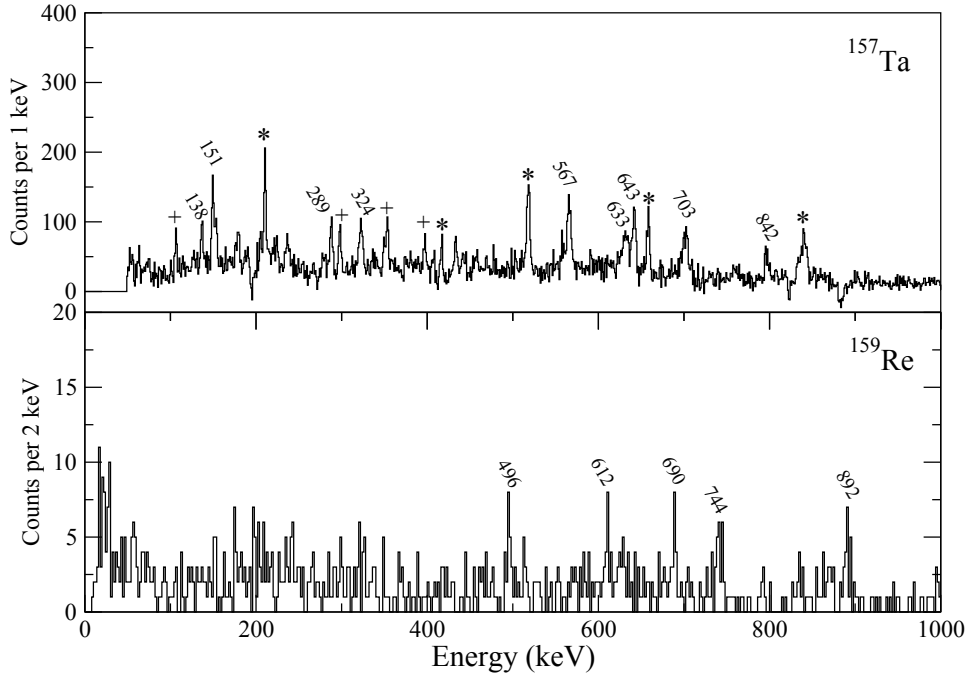

Figure 7.1: *Top: γ rays in coincidence with the implantation of a recoil-^{157}Ta correlation. Despite a background subtraction the spectrum is heavily contaminated. Transitions due to ^{159}W (which has an αdecay energy which overlaps with ^{159}Re) are labelled with asterisks [56]. Transitions due to ^{155}Lu (which is very heavily populated in this reaction and has a high energy αdecay which can be erroneously assigned as a ^{159}Re decay when the αfails to deposit its full energy) are labelled with crosses [57]. Despite the contamination all of the ^{157}Ta transitions identified in reference [16] are visible, including the 151 keV transition absent from the ^{159}Re spectrum. Bottom: the same spectrum as shown in figure 6.4, i.e. rays assosciated with with the $h_{11/2}$ state of ^{159}Re.*

in reference [16] and shown figure 7.2, in which the lowest-lying transitions feeding the $h_{11/2}$ state were 847, 703 and 151 keV, with the ordering based on intensity arguments. By comparison to the ^{157}Ta level scheme the 892 and 744 keV transitions are likely to be the lowest lying transitions in ^{159}Re. There is not, however, any candidate that corresponds to the 151 keV transition seen in ^{157}Ta. The upper part of figure 7.1 shows a spectrum of γ rays that are temporally correlated with a ^{157}Ta implantation obtained in the present experiment by tagging on the 6213 keV α decay [14]. Despite a background

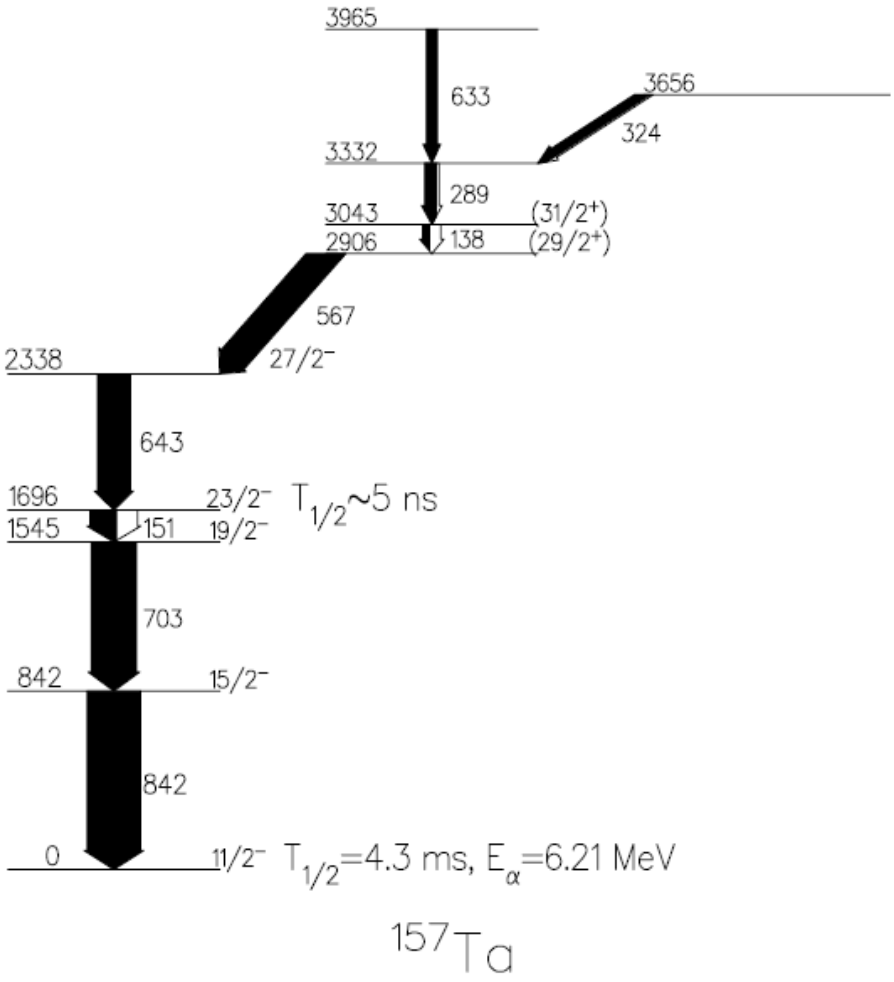

Figure 7.2: *Level scheme for* ^{157}*Ta, taken from reference [16].*

subtraction this spectrum remains heavily contaminated with ^{159}W γ rays due primarily to the proximate nature of the ^{159}W α decay. Nonetheless all of the γ rays identified in reference [16] can be seen. This confirms that the absence of a low energy transition in the ^{159}Re spectrum is not due to some facet of these data which causes transitions in this region to be lost, but rather suggests that an analogue of the 150 keV transition does not exist, indicating some change of structure between the isotones.

Figure 7.3 shows the excitation energies of the low lying states above the $h_{11/2}$ state for the odd-Z N=84 isotones, including the values for ^{159}Re from this

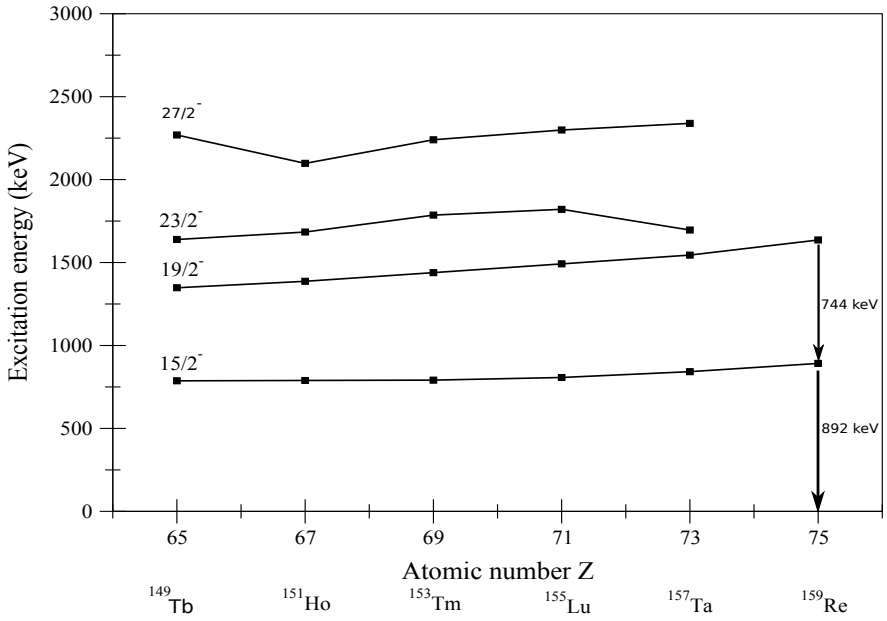

Figure 7.3: *Excitation energies relative to the $h_{11/2}$ state of the odd-Z N=84 isotones as a function of proton number. The values for ^{159}Re are from this work. Other values are from references [16], [58], [59], [60] and [57].*

work, with the transition energies shown for clarity. The steadily increasing excitation energy of the $15/2^-$ and $19/2^-$ states is symptomatic of the decreasing deformation as the odd proton decouples from the 2^+ and 4^+ excitations of the near spherical core.

Chapter 8

Summary

A tentative assignment for the α decay of the highly neutron deficient N=84 isotone ^{160}Os has been made using recoil-mother-daughter correlations. Correlations with ^{156}Hf, ^{156m}Hf and ^{156}Ta decay modes have been analysed with the best signal-to-background ratio occurring when the ^{156}Ta correlation is omitted. The expected background activity due to false correlations has been analysed and found to be below the observed signal and an analysis using the LISA spectrometer confirmed that the signal is consistent with a pure neutron channel. The measured Q-value of 7415(50) keV is approximately 100 keV higher than would be expected from systematics and physical explanations for this discrepancy have been discussed. The half-life has been measured to be 35^{+19}_{-15} μs using a maximum likelihood method and is consistent with the observed Q-value and inconsistent with the expected half-life of the background. However the measured α-α time differences are more consistent with background than signal, and the expected 8^+ isomer has not been observed. Overall the assignment is promising but confirmation of this result requires further work, to which end 14 days of beam time has been approved for a further experiment at the University of Jyväskylä. The experiment will employ

the vacuum mode separator MARA in place of RITU, which will be capable of separating reaction products by mass, and the veto detector UoYtube which will offer an order of magnitude improvement on charged particle vetoing efficiency compared to LISA. Other improvements include greater segmentation of the silicon strip detector (reducing false correlations), the use of digital electronics which will reduce dead time in the silicon detector to <1 μs, and a beam energy optimised for the production ^{160}Os.

Improved measurements of the $h_{11/2}$ state in ^{159}Re and its daughter, ^{155}Ta, have been made using mother-daughter correlations, and the results are consistent with previous works. Six γ rays above the $h_{11/2}$ state in ^{159}Re have been identified using γ ray spectroscopy and background reduction techniques, including the use of add-back in the PIN diodes. The 892 keV and 744 keV transitions have been assigned as the lowest lying transitions based on comparisons to the N=84 isotone ^{157}Ta. Statistics were not sufficient to allow $\gamma-\gamma$ coincidence measurement to assign an order to the other transitions. Evidence for a $25/2^-$ α-decaying isomer has been found, in which activity that is consistent with the proton decay of ^{155}Ta arises when looking at events that are preceded by an event in the high energy portion of the ^{156}Hf 8^+ isomer, behind which it is possible that the ^{159}Re isomer lies. However the activity is within the range of statistical fluctuations and it is not possible to isolate the signal using an analysis of the life times due to the expected similarity between the half-lives of the ^{159}Re and ^{156}Hf isomers. The planned experiment to search for ^{160}Os will utilise a reaction and beam energy that will also produce ^{159}Re nuclei, and the same experimental improvements that will allow for reduced background in that analysis will be applicable to ^{159}Re.

In addition to the search for ^{160}Os MARA will be used in a wider programme of discovery and characterisation of nuclei close to (or beyond) the

proton drip line. Current proposals include the search for two new isotopes (^{165}Pt and ^{169}Au) and spectroscopy of ^{176,177}Tl in a proton-tagged RDT experiment.

Bibliography

[1] M. Drummond, PhD thesis (2013).

[2] L. Bianco *et al.*, Phys. Lett. B **690**, 15 (2010).

[3] R. Robinson and M. Thoennessen, Atomic Data and Nuclear Data Tables **98**, 911 (2012).

[4] NuDat 2.6 nuclear data cards. http://www.nndc.bnl.gov/nudat2/. Date accessed 20/01/2017 .

[5] P. Moller, J. Nix, and K.-L. Kratz, Atomic Data and Nuclear Data Tables **66**, 131 (1997).

[6] D. Joss *et al.*, Phy. Lett. B **641**, 34 (2006).

[7] R. D. Page *et al.*, Phys. Rev. C **75**, 061302(R) (2007).

[8] J. Uusitalo *et al.*, Phys. Rev. C **59** (19999).

[9] S. Åberg, P. Semmes, and W. Nazarewicz, Phys. Rev. C **56** (1997).

[10] P. Moller, A. J. Sierk, T. Ichikawa, and S. Sagawa, At. Data and Nucl. Data Tables **109-110** (2016).

[11] S. Goriely, M. Samyn, and J. M. Pearson, Phys. Rev. C **75** (2007).

[12] P. Kleinheinz *et al.*, Z. Physik A **290** (1979).

[13] H. Mahmud *et al.*, Phys. Rev. C **62**, 057303 (2000).

[14] R. D. Page *et al.*, Phys. Rev. C **53**, 660 (1996).

[15] S. Hofmann *et al.*, Z. Phys. A **291**, 53 (1979).

[16] D. Seweryniak *et al.*, Phys. Rev. C **71**, 054319 (2005).

[17] D. Joss *et al.*, Phys. Lett. B **772**, 703 (2017).

[18] C. R. Bingham *et al.*, Phys. Rev. C **54**, R20 (1996).

[19] K. S. Krane, *Introductory Nuclear Physics* (John Wiley and Sons, 1988).

[20] R. F. Casten, *Nuclear Structure from a Simple Perspective* (Oxford University Press, 2000).

[21] J. O. Rasmussen, Phys. Rev. **113**, 1593 (1959).

[22] A. H. Wapstra, *Nuclear spectroscopy tables* (Amsterdam, 1959).

[23] V. F. Weisskopf, Phys. Rev. **83**, 1073 (1951).

[24] C. W. Beausang and J. Simpson, J. Phys. G: Nucl. Part. Phys **22**, 527 (1996).

[25] G. Duchnea *et al.*, Nuclear Instruments and Methods in Physics Research A **432**, 90 (1999).

[26] STFC Nuclear Physics Group website http://npg.dl.ac.uk/Lisa/Photos/. Date accessed 22/08/2017. .

[27] STFC technologies website https://www.technologysi.stfc.ac.uk/Pages/NPG-LISA.aspx. Date accessed 22/08/2017 .

[28] P. Greenlees, PhD thesis (1999).

[29] R. Page *et al.*, Nuclear Instruments and Methods in Physics Research B **204**, 634637 (2003).

[30] I. H. Lazarus *et al.*, IEEE TRANSACTIONS ON NUCLEAR SCIENCE **48**, 567 (2001).

[31] P. Rahkila, Nuclear Instruments and Methods in Physics Research A **595**, 638 (2008).

[32] O. Tarasov and D. Bazin, Nuclear Instrumentation and Methods in Physics Research B **204**, 174 (2003).

[33] J. Revill, Private communication.

[34] A. Korgul *et al.*, Phys. Rev. C **77**, 034301 (2008).

[35] I. G. Darby *et al.*, Phys. Rev. C **83**, 064320 (2011).

[36] R. J. Irvine *et al.*, Phys. Rev. C **55**, R1621 (1997).

[37] H. Kettunen *et al.*, Phys. Rev. C **69**, 054323 (2004).

[38] C. N. Davids *et al.*, Phys. Rev. C **55**, 2255 (1997).

[39] S. Hofmann *et al.*, Z. Phys. A **299**, 281 (1981).

[40] S. Hofmann *et al.*, Z. Phys. A **333**, 107 (1989).

[41] A. Rytz, Atomic Data and Nuclear Data Tables **47**, 205 (1991).

[42] S. D. Negra, C. Deprun, D. Jacquet, and Y. L. Beyec, Annales de Physique (Paris) **7**, 149 (1982).

[43] K. S. Toth, W. D. Schmidt-Ott, C. R. Bingham, , and M. A. Ijaz, Phys. Rev. C **12**, 533 (1975).

[44] D. Eastham and I. Grant, Nucl. Phys. A **208**, 119 (1973).

[45] T. Hild *et al.*, Phys. Rev. C **51**, 1736 (1995).

[46] C. Cabot, S. D. Negra, C. Deprun, H. Gauvin, and Y. L. Beyec, Z. Phys. A **287**, 71 (1978).

[47] C. Cabot *et al.*, Nucl. Phys. A **241**, 341 (1975).

[48] H. A. Enge *et al.*, Phys. Rev. C **25**, 1830 (1982).

[49] J. Uusitalo *et al.*, Z. Phys. A **358**, 375 (1997).

[50] B. Hadinia *et al.*, Phys. Rev. C **80**, 064310 (2009).

[51] A. Thornthwaite *et al.*, Phys. Rev. C **86**, 064315 (2012).

[52] G. J. Feldman and R. Cousins, Phys. Rev. D **57**, 3873 (1998).

[53] S. L. Meyer, *Data Analysis for Scientists and Engineers* (New York: J. Wiley, 1975).

[54] K. H. Schmidt, C. C. Sahm, K. Pielenz, and H.-G. Clerc, Z. Phys. A **316** (1984).

[55] K. Heyde and J. L. Wood, Rev. Mod. Phys. **83**, 1467 (2011).

[56] P. J. Sapple *et al.*, Phys. Rev. C **84**, 054303 (2011).

[57] R. Carroll, PhD thesis (2012).

[58] M. Lach *et al.*, Z. Phys. A **341** (1991).

[59] J. Gizon *et al.*, Z. Phys. A **301** (1981).

[60] C. Zhang *et al.*, Z. Phys. A **348** (1994).